Cell Metabolism

Resource

MARIGOLD and MitoCIAO, two searchable compendia to visualize and functionalize protein complexes during mitochondrial remodeling

Graphical abstract

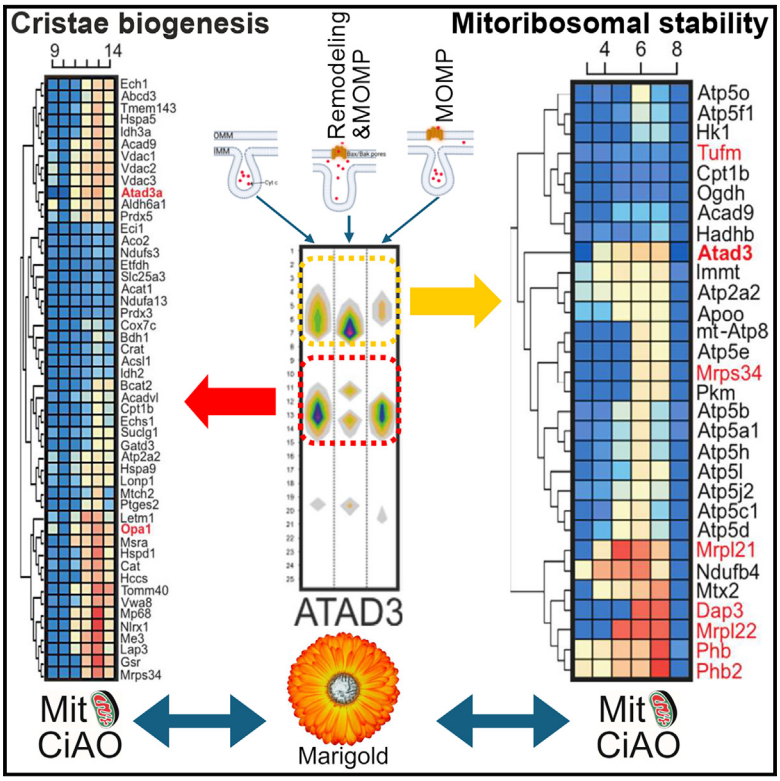

Highlights

- MARIGOLD visualizes dynamics of protein complexes during mitochondrial remodeling
- MitoCIAO predicts protein interactions in complexes using computational tools
- MitoCIAO predictions are validated by biologically confirmed interactions
- MARIGOLD & MitoCIAO reveal two ATAD3A complexes for cristae and mitoribosome stability

Authors

Giovanni Rigoni, Enrique Calvo, Christina Glytsou, ..., Jose Antonio Enriquez, Luca Scorrano, Maria Eugenia Soriano

Correspondence

luca.scorrano@unipd.it (L.S.), mariaeugenia.soriano@unipd.it (M.E.S.)

In brief

Rigoni et al. use complexomic to develop two online-available tools, MARIGOLD and MitoCIAO, mapping mitochondrial protein interactions during membrane remodeling. MARIGOLD provides "digital western blots" of queried proteins in their native complexes. MitoCIAO predicts their comigrating partners. These tools deorphanize two ATAD3A-containing complexes participating in cristae biogenesis and mitoribosome stability.

Rigoni et al., 2025, Cell Metabolism *37*, 1024–1038
April 1, 2025
https://doi.org/10.1016/j.cmet.2025.01.017

CellPress

CellPress
OPEN ACCESS

Cell Metabolism

Resource

MARIGOLD and MitoCIAO, two searchable compendia to visualize and functionalize protein complexes during mitochondrial remodeling

Giovanni Rigoni,[1,9,10] Enrique Calvo,[2,3,9] Christina Glytsou,[1,4,9,11] Marta Carro-Alvarellos,[1] Masafumi Noguchi,[1,4,12] Martina Semenzato,[1,4] Charlotte Quirin,[1,4] Federico Caicci,[1] Natascia Meneghetti,[5] Mattia Sturlese,[6] Takaya Ishihara,[7] Stefano Moro,[6] Chiara Rampazzo,[1] Naotada Ishihara,[7] Fabrizio Bezzo,[5] Leonardo Salviati,[8] Jesùs Vazquez,[2,3] Gabriele Sales,[1] Chiara Romualdi,[1] Jose Antonio Enriquez,[2] Luca Scorrano,[1,4,*] and Maria Eugenia Soriano[1,13,*]

[1]Department of Biology, University of Padova, Via U. Bassi 58B, 35121 Padova, Italy
[2]Centro Nacional de Investigaciones Cardiovasculares Carlos III, 28029 Madrid, Spain
[3]CIBER de Enfermedades Cardiovasculares, 28029 Madrid, Spain
[4]Veneto Institute of Molecular Medicine, 35129 Padova, Italy
[5]CAPE-Lab, Department of Industrial Engineering, University of Padova, Padova, Italy
[6]Department of Pharmaceutical Sciences, University of Padova, 35131 Padova, Italy
[7]Department of Biological Sciences, Graduate School of Science, Osaka University, 560-0043 Toyonaka, Japan
[8]Department of Women's and Children's health, University of Padova and IRP Città della Speranza, 35127 Padova, Italy
[9]These authors contributed equally
[10]Present address: Max Planck Institute for Multidisciplinary Sciences, Research Group Structure and Dynamics of Mitochondria, 37077 Göttingen, Germany
[11]Present address: Department of Pediatrics, Robert Wood Johnson Medical School, Department of Chemical Biology, Ernest Mario School of Pharmacy, Rutgers University, Piscataway, NJ 08854, USA
[12]Present address: Laboratory of Pharmacology, School of Pharmaceutical Sciences, Wakayama Medical University, Wakayama 640-8156, Japan
[13]Lead contact
*Correspondence: luca.scorrano@unipd.it (L.S.), mariaeugenia.soriano@unipd.it (M.E.S.)
https://doi.org/10.1016/j.cmet.2025.01.017

SUMMARY

Mitochondrial proteins assemble dynamically in high molecular weight complexes essential for their functions. We generated and validated two searchable compendia of these mitochondrial complexes. Following identification by mass spectrometry of proteins in complexes separated using blue-native gel electrophoresis from unperturbed, cristae-remodeled, and outer membrane-permeabilized mitochondria, we created MARIGOLD, a mitochondrial apoptotic remodeling complexome database of 627 proteins. MARIGOLD elucidates how dynamically proteins distribute in complexes upon mitochondrial membrane remodeling. From MARIGOLD, we developed MitoCIAO, a mitochondrial complexes interactome tool that, by statistical correlation, calculates the likelihood of protein cooccurrence in complexes. MitoCIAO correctly predicted biologically validated interactions among components of the mitochondrial cristae organization system (MICOS) and optic atrophy 1 (OPA1) complexes. We used MitoCIAO to functionalize two ATPase family AAA domain-containing 3A (ATAD3A) complexes: one with OPA1 that regulates mitochondrial ultrastructure and the second containing ribosomal proteins that is essential for mitoribosome stability. These compendia reveal the dynamic nature of mitochondrial complexes and enable their functionalization.

INTRODUCTION

Mitochondria are functionally and morphologically plastic. Often, these two facets are linked, structural changes leading to functional outcomes and vice versa. This form-function relationship was originally discovered in mitochondria undergoing morphological transitions upon stimulation of respiration.[1] Later, it was extended to apoptosis, where mitochondrial cristae remodel and mitochondrial network fragments to release cytochrome c.[2,3] Because mitochondrial morphology and ultrastructure are controlled by mitochondria-shaping proteins, genetic experiments are possible to precisely functionalize mitochondrial morphological changes.[4] The use of genetics not only confirmed that morphology changes are necessary for efficient mitochondrial respiration as originally described but also identified the stability of respiratory chain supercomplexes (RCS), quaternary assemblies of respiratory chain complexes (RCC), as the functional effectors of mitochondrial remodeling for respiration.[5] The

discovery that mitochondrial morphology can modulate the ratio between RCS and RCC and hence respiration nominated mitochondrial high molecular weight (HMW) complexes as effectors of the form-function relationship for these organelles.

Mitochondrial proteome consists of ~1,100 proteins identified with high confidence in subsequent studies stemming from the original MitoCarta (now MitoCarta 3.0[6,7]) and multidimensionally explored for their relative abundance and stability.[8] Remarkably, cristae of mitochondria from post-mitotic cells harbor a large number of long-lived proteins, raising the interesting possibility that mitochondrial functional plasticity might be linked to dynamic changes in mitochondrial HMW complexes.[9] Indeed, complexome analysis, i.e., the analysis by liquid chromatography/mass spectrometry (LC-MS) or iBAQ of proteins in mitochondrial complexes separated by blue-native polyacrylamide gel electrophoresis (BNGE), revealed changes in several HMW complexes in cells devoid of mtDNA.[10,11] However, comparative complexomic analyses on mitochondria from established cell lines do not capture whether HMW complex composition can be rapidly influenced, e.g., by changes in mitochondrial metabolism, in membrane shape, or by the recruitment of mitochondria in the apoptotic signaling cascade.

Apoptosis provides an interesting paradigm where mitochondrial membrane remodeling leads to changes in mitochondrial HMW complexes. During mitochondrial outer membrane permeabilization (MOMP) proapoptotic members of the Bcl-2 family, like BAX and BAK, assemble in large complexes in the outer membrane.[12,13] At the level of the inner membrane, proapoptotic stimuli that induce BAX/BAK oligomerization induce the parallel destabilization of HMW complexes containing optic atrophy 1 (OPA1) to remodel mitochondrial cristae.[14–17] OPA1 belongs to the family of the large dynamin-related GTPases proteins. These proteins include the pro-fusion mitofusins 1 and 2 (MFN1/2) and the pro-fission dynamin-related protein 1 (DRP1). On mitochondria, DRP1 uses as receptors mitochondrial fission factor (MFF), fission protein 1 (FIS1), and mitochondrial division 49 and 51 (MiD49/51). In addition, OPA1 together with the large multimeric complex known as mitochondrial cristae organization system (MICOS) and the ATP synthase organize mitochondrial cristae.[4] Reciprocally, changes in membrane shape can affect respiratory chain HMW supercomplexes[5] as well as the MICOS complex and ATP synthase dimerization.[15,16] These results suggest that apoptosis and cristae remodeling can be leveraged to systematically inspect the dynamic behavior of mitochondrial complexes and hence to generate testable hypotheses on their function in mitochondrial physiology.

We performed a systematic analysis of HMW complexes in mouse heart mitochondria undergoing remodeling and MOMP. By combining BNGE with tandem MS with data-independent scanning (DiS), we generated Mitochondrial_Apoptotic_RemodelInG_cOmpLexome Database (MARIGOLD), a database of the relative distribution of 626 proteins in HMW complexes. We leveraged MARIGOLD to generate MitoCIAO, a second database predicting protein cooccurrence in HMW complexes using a statistical correlation approach. Both MARIGOLD and MitoCIAO are available online (https://mitociao.bio.unipd.it/). We validated MitoCIAO by assigning two genetically distinguishable functions to two ATAD3A-containing mitochondrial HMW complexes.

RESULTS

MARIGOLD, a searchable Mitochondrial Apoptotic RemodelInG cOmpLexome Database

To identify dynamic changes in mitochondrial complexes during MOMP and cristae remodeling, we used a reconstituted system of respiring mitochondria isolated from C57Bl/6 mouse hearts and recombinant active BID (cBID). To dissociate MOMP from cristae remodeling, we used the cBID^{KKAA} mutant that permeabilizes the outer membrane but does not induce cristae remodeling[5] (Figure 1A). We separated by BNGE digitonin-extracted mitochondrial complexes from the three experimental conditions (untreated, treated with cBID, and treated with cBID^{KKAA}), using a digitonin concentration that preserves RCS and ATP synthase oligomers, to avoid detergent-induced changes in the relative complex organization.[15,16] Each gel lane from the 3 conditions was then sliced in parallel into 25 bands, numbered 1 to 25 from the top to the bottom of the gel. Bands from three independent experiments were pooled and processed as a single sample by LC/MS using DiS. We identified the corresponding proteins by comparing the retrieved peptides to *M. musculus* as well as *R. norvegicus* reference databases to avoid issues with peptides that might not be represented in the mouse database. This proteomic analysis identified a total of 1,105 proteins with a substantial contamination from other cellular compartments (Figure 1B). We expected this degree of contamination because we had chosen not to use Percoll-purified mitochondria. Indeed, we were also interested in changes in complexes representing potential bridges between mitochondria and other organelles such as the endoplasmic reticulum (ER) that participates in apoptosis and is required to augment BID-mediated MOMP.[18] Therefore, we filtered the list of proteins using MitoMiner 4.0 (https://mitominer.mrc-mbu.cam.ac.uk/release-4.0/begin), setting a threshold in the integrated mitochondrial protein import (IMPI) score >0.5.[19] Furthermore, we manually filtered the list to retain proteins annotated to be mitochondrial even if they lacked an IMPI score in MitoMiner. Thus, we obtained MARIGOLD, a Mitochondrial Apoptotic RemodelInG cOmpLexome Database composed of 627 proteins (Figure 1B). Each protein is accompanied in MARIGOLD by the number of peptide spectrum matches (PSMs) retrieved in each individual slice from the BNGE in the 3 different experimental conditions (Data S1). MARIGOLD was mostly populated by proteins described as mitochondrial (85.2%), with a minority of proteins found from other organelles (12.3%) or with unknown location (2.5%) (Figure 1B). MARIGOLD is available online at https://mitociao.bio.unipd.it/ and can be searched by typing the Uniprot gene name of the protein of interest. In response, the user obtains a downloadable color-coded contour plot for the queried protein, representing the PSMs retrieved in each slice. Because slices correspond to a defined position in the BNGE, apparent MW markers are also included in the plot. This graphical output informs the user about the *relative* abundance of the PSMs assigned to the protein of interest in different complexes of different sizes in resting, permeabilized, and remodeled mitochondria.

Using MARIGOLD, we generated MitoCIAO, a Mitochondrial Complexes InterActome tOol. MitoCIAO is a searchable online tool that reports the comigration likelihood estimate of individual proteins in complexes from the three experimental conditions.

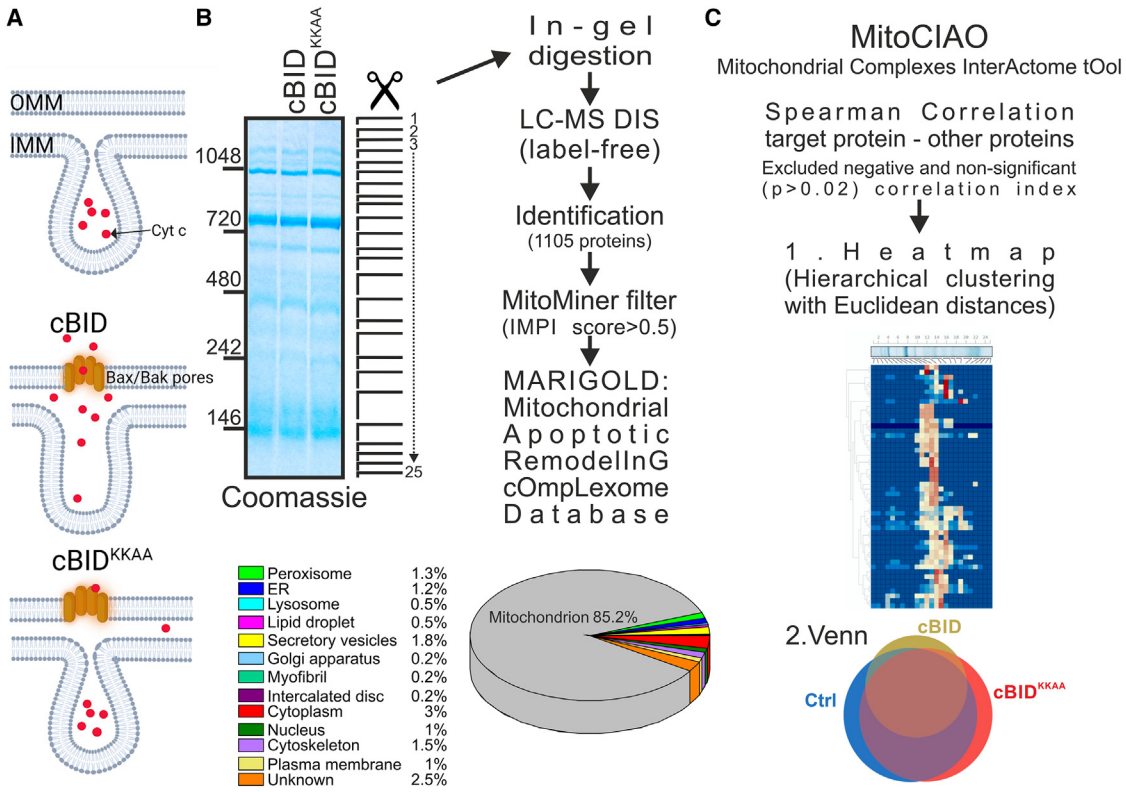

Figure 1. Workflow of MARIGOLD and MitoCIAO generation

(A) Illustration describing the effects of cBID and cBID^{KKAA} on mitochondrial cristae and MOMP.

(B) Coomassie staining after BNGE of mitochondrial protein complexes extracted from mitochondria isolated from mouse heart and untreated or treated with cBID or cBID^{KKAA} (n = 3 technical replicates from 3 biological replicates for each condition) The lines on the right identify the bands sliced (1–25) and separately digested with trypsin before label-free analysis by LC-MS DiS, which led to the identification of 1,105 proteins. MitoMiner filtering was used to exclude proteins with an IMPI score $\leq$ 0.5. From this analysis, we obtained the Mitochondrial Apoptotic RemodelInG cOmpLexome Database (MARIGOLD). MARIGOLD includes mostly mitochondrial proteins as well as proteins assigned to organelles and compartments illustrated in the pie graph.

(C) Description of the mitochondrial complexes interactome tool (MitoCIAO) generation based on the Spearman correlation between the protein of interest and the other proteins present in the database. The interaction is represented as (1) heatmaps with hierarchical clustering and Euclidean distances and (2) a Venn diagram showing putative interactors of the target protein in one or more of the experimental conditions indicated.

Existing complexome databases from mammalian and plant mitochondria are curated catalogs where PSMs of a given protein are assigned to each slice of the processed BNGE, similar to MARIGOLD.[10] In MitoCIAO we estimate the likelihood of comigration between the queried protein and all the other proteins identified in MARIGOLD. Using an ad hoc R script, MitoCIAO calculates the distribution of the PSMs for each individual protein in the BNGE slices and computes the Spearman correlation index (ρ) between each protein and all the other proteins listed by MARIGOLD in any given BNGE slice. MitoCIAO therefore reports ρ values between the queried protein and the other proteins. The user can select the p value threshold used to compute ρ. These ρ values are used to generate heatmaps and hierarchically clustered with Euclidean distances to provide a visual output of the likelihood of comigration between the protein of interest and each other protein in each slice of the BNGE. Because detected PSMs might differ among different proteins, we normalized PSMs to the total PSMs identified for the given protein along the BNGE lane in each treatment and converted them to a color gradient from blue (0, no PSMs) to red (1, highest number of PSMs counts relative to the total identified). Uniprot gene names of the identified, likely comigrating proteins are listed and clickable, linking to the Uniprot page of the protein that opens in a new browser window. Heatmaps are presented for unperturbed as well as for cBID- and cBID^{KKAA}-treated mitochondria so that the user can appreciate changes in the likelihood of comigration in these three different conditions. Furthermore, MitoCIAO also plots a Venn diagram that includes the proteins correlating with the queried protein in each of the treatments as well as in their intersections. By clicking on the individual areas of the Venn diagram, a popup opens with the list of the Uniprot gene names of the proteins correlating with the queried one (Figure 1C). Finally, csv tables of raw ρ and p values are downloadable from the same page.

MitoCIAO successfully predicts interactions among proteins in HMW complexes of the inner mitochondrial membrane

We road-tested MitoCIAO's ability to predict protein-protein interactions in HMW complexes by searching for the core MICOS component MIC60 (IMMT) that regulates cristae junction formation and stability and is targeted by cBID.[15,20] Several

interactors of MIC60 have been previously identified. MitoCIAO returned three heatmaps of the potential IMMT interactors in unperturbed, remodeled, and permeabilized mitochondria (Figure S1A). These heatmaps as well as the Venn diagram subdivision corresponding to predicted IMMT interactors in all three conditions contained most of the MICOS proteins known to interact with IMMT: CHCHD3 (MIC19),[21] MIC13 (Qil1),[22,23] APOOL (MIC27), as well as DNAJC11, MTX1, MTX2, and SAMM50[24] (Figure S1B). We therefore used MARIGOLD to analyze CHCHD3, APOOL, DNAJC11, MIC13, MTX1, MTX2, and SAMM50 distribution. All these proteins were retrieved in complexes running at the same MW of IMMT (Figure S1C). We identified three main complexes containing IMMT, CHCHD3, APOOL, and DNAJC11. These complexes were targeted by cBID but not by cBID^{KKAA}, suggesting their involvement in cristae morphology. MIC13 migrated in a main complex with IMMT, CHCHD3, and APOOL. Because this complex was not targeted by cBID, we posit the existence of a very stable MIC13-containing subcomplex not affected by cristae remodeling (Figure S1C).

We finally performed a reciprocal analysis by querying in MitoCIAO the MICOS components identified as potential IMMT interactors. The obtained putative interactors were different depending on the protein, suggesting that not all the MICOS components interact with each other and identifying potential subassemblies as the ones described in previous studies.[21,25,26] Our analysis predicted the following interactions: IMMT with CHCHD3, SAMM50, MIC13, DNAJC11, APOOL, and MTX1; CHCHD3 with IMMT, SAMM50, MIC13, DNAJC11, APOOL, and MTX1; MIC13 with IMMT, CHCHD3, and APOOL; APOOL with IMMT, CHCHD3, MIC13, and SAMM50; and SAMM50 with IMMT, CHCHD3, DNAJC11, APOOL, and MTX2. MitoCIAO identifies IMMT and CHCHD3 as the core complex where all the other identified partners seem to assemble, likely by forming subcomplexes, as supported by the MARIGOLD contour plots (Table S1). We therefore used these MitoCIAO predictions to draw an interaction model of the different MICOS components (Figure S1D). Our model resembles the ones previously proposed based on genetic, biochemical, and functional approaches.[21,27] Altogether, MitoCIAO can predict interactions among MICOS components that have been validated in the wet lab and, in combination with MARIGOLD, can identify MICOS subassemblies that respond differentially to mitochondrial remodeling, suggesting their participation in mitochondrial processes other than cristae biogenesis.

MitoCIAO identifies putative interactors of OPA1

After validating MitoCIAO and MARIGOLD against the well-characterized MICOS complex, we next wished to exploit its potential as a discovery tool by exploring the dynamic complexes of OPA1, another key cristae regulator.[14,15] We therefore queried MitoCIAO for OPA1 and obtained the hierarchically clustered heatmaps of the top 50 candidate OPA1 interactors (Figure 2A). By inspecting the Venn diagram listing the cooccurrence of the putative interactors identified in the three experimental conditions, we noticed that most OPA1 potential interactors concentrated in the intersection between control- and cBID^{KKAA}-treated mitochondria (42 potential interactors) as well as in the intersection among the 3 conditions (56 potential interactors) (Figure 2B). We reasoned that this latter list would encompass "stable" OPA1 interactors, whereas the former list would include proteins that likely comigrate with OPA1 when cristae are intact but not when they are remodeled. Hence, we concentrated on these two lists of putative OPA1 interactors, and we found proteins known to interact with OPA1 from pull-down and MS analysis, like SLC25A12, SLC25A13, TOM40, MIC19, MIC60, ATAD3A, and ATP synthase subunits.[15,16,28,29] We again went back to MARIGOLD to inspect the changes in the distribution of selected proteins from these two groups in response to MOMP and mitochondrial remodeling. We noticed the existence of three different distribution profiles: proteins like LETM1 (Leucine zipper-, EF-hand-containing transmembrane protein 1) and VWA8 (Von Willebrandt containing 8) that belong to the stable OPA1 interactors were found in two main HMW complexes where OPA1 was also retrieved and that followed the same fate of OPA1 upon cristae remodeling (black and red boxes in Figure 2C). The second distribution profile was characteristic of other stable OPA1 putative interactors, like CCDC51 (the mitochondrial K_{ATP} channel) and MCUR1 (mitochondrial calcium uniporter regulator 1), that were retrieved only in one HMW and responded to cristae remodeling like OPA1. The third distribution profile contained TMEM143 (a stable OPA1 interactor), with OPA3 and ATAD3A that are among the proteins interacting with OPA1 only when cristae are not remodeled. TMEM143 and OPA3 were mainly retrieved in two different HMW complexes: the complex containing OPA1, where they responded like OPA1 to cristae remodeling and MOMP, and a second complex running at the lowest MW that was insensitive to mitochondrial perturbation (green box in Figure 2C). ATAD3A was retrieved in these two complexes but also in a complex at a higher MW (~1 MDa) that caught our attention to further validate our tools because it was abundant and did not decrease in cBID-treated samples, suggesting its involvement in a different process not directly regulating cristae remodeling.

MARIGOLD and MitoCIAO identify OPA1 among the putative interactors of ATAD3A

Because the ATAD3A-containing complexes only partially overlapped with those containing OPA1 in MARIGOLD, we wanted to confirm the predictive ability of our database. We therefore turned to MitoCIAO and searched for ATAD3A at a $p < 0.05$ stringency and restricted the analysis to the ~500 kDa complex (corresponding to the BNGE slices 9–14) where both ATAD3A and OPA1 were retrieved. As expected, we obtained three different heatmaps showing the putative ATAD3A interactors in each experimental condition (Figure 3A). In the Venn diagram intersection describing the ATAD3A interactors common among control-, cBID-, and cBID^{KKAA}-treated mitochondria, we retrieved OPA1, LETM1, and LONP1 (Figure 3B) that displayed the same distribution profile in MARIGOLD. Thus, MitoCIAO confirms the possibility that OPA1 and ATAD3A are retrieved in a ~500 kDa HMW complex.

We next wished to validate the predicted comigration between OPA1 and ATAD3A in the ~500 kDa complex that decreased during apoptotic cristae remodeling. Immunoblot analysis after BNGE (Figure 3C) and 2D BNGE-SDS-PAGE (Figure 3D) confirmed that levels of ATAD3A in this complex decreased upon cBID-induced cristae remodeling. We further validated

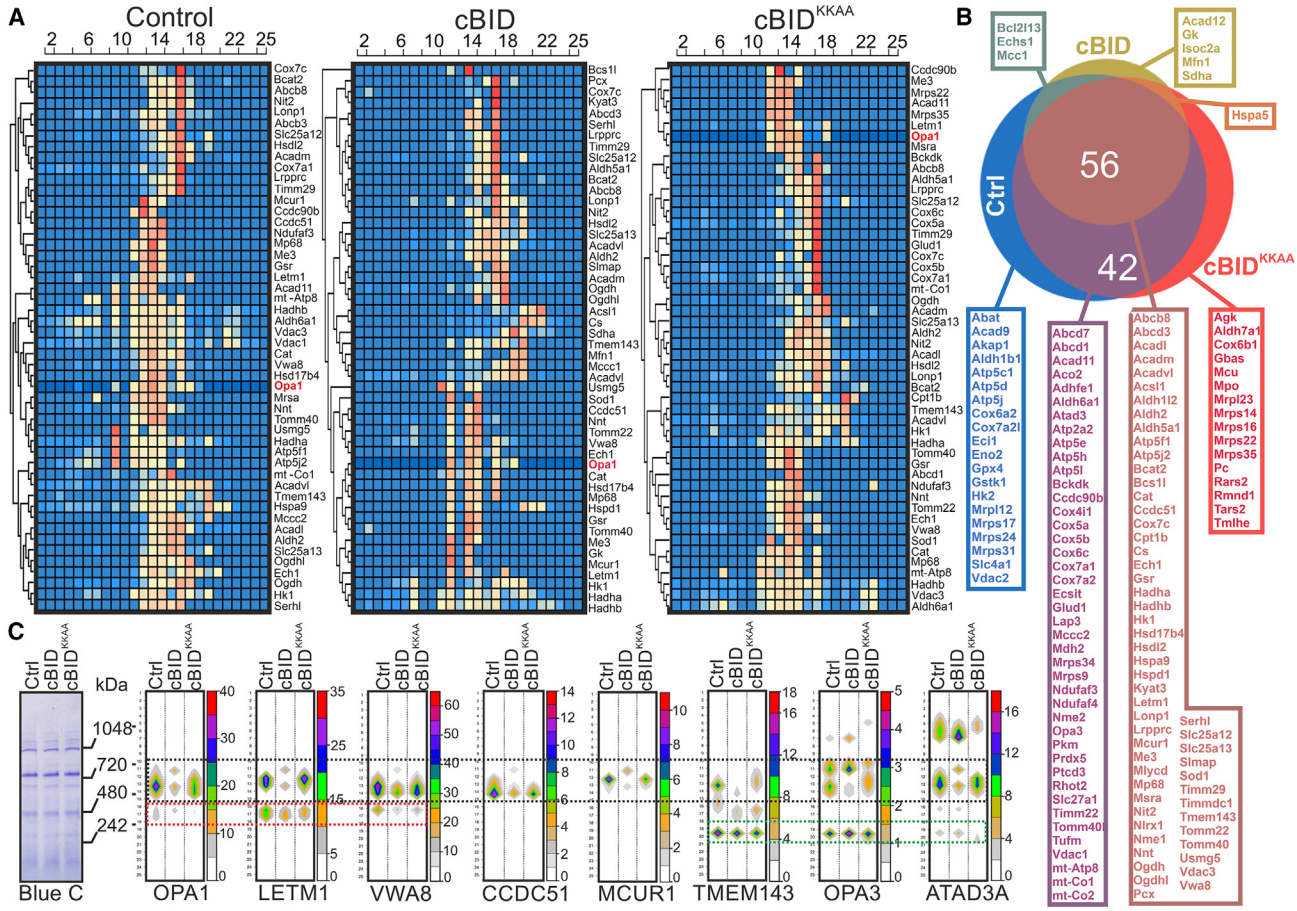

Figure 2. OPA1 interactome analysis with MitoCIAO

(A) Heatmaps and hierarchical clustering of fifty OPA1 putative interactors at the p value ≤ 0.05 threshold in mouse heart mitochondria treated as indicated in the BNGE slices 1–25 as indicated above the heatmaps. The color scale indicates the normalized PSM distribution of each individual protein.

(B) Venn diagram of the proteins identified as putative interactors of OPA1 in experiments as in (A). In each Venn area, the number of putative interactors and their gene name are indicated.

(C) Coomassie-stained BNGE and color-coded violin plots of protein distribution of representative putative OPA1 interactors in heart mitochondria treated as indicated (n = 3 technical replicates from 3 biological replicates for each condition). Color scale represents the number of PSMs for each individual protein. Common complexes between putative interactors are evidenced with dotted squares.

this result after apoptotic induction with the BH3-mimetic ABT737. Also in this case, the ~500 kDa complex containing ATAD3A and OPA1 is highly affected (Figure S2). Moreover, coimmunoprecipitation (coIP) experiments indicated that OPA1 physically interacts with endogenous or overexpressed HA-tagged ATAD3A (Figures 3E and 3F). Overall, these results indicate the ability of MitoCIAO to predict the comigration between OPA1 and ATAD3A in an HMW complex targeted during apoptotic cristae remodeling.

A functional ATPase domain of ATAD3A is required for cristae biogenesis

The validated prediction by MitoCIAO that OPA1-ATAD3A comigrates in the ~500 kDa HMW complex pointed to a role for ATAD3A in the regulation of cristae shape. Indeed, this OPA1-containing complex is targeted during cristae remodeling and stabilized by the OPA1 overexpression.[14,30] Moreover, ATAD3A downregulation results in aberrant cristae morphology by an unclear mechanism.[31] We therefore decided to verify whether ATAD3A participates in cristae shape organization via this ~500 kDa complex. We first confirmed that we could achieve efficient ATAD3A downregulation or overexpression in MAFs (Figures S3A and S3B). Silencing of ATAD3A reduced cristae number and increased cristae lumen width (CLW). Conversely, overexpression of mouse ATAD3A did not further increase cristae number, but it decreased CLW, similar to what was observed upon OPA1 overexpression (representative EMs in Figures S3C and quantification in S3D and S3E).[15] Moreover, ATAD3A downregulation was accompanied by mitochondria fragmentation, whereas ATAD3A overexpression did not induce elongation (Figures S3F and S3G). Altogether, these data indicate that, as expected, ATAD3A ablation impairs cristae biogenesis but did not clarify whether this was due to the disruption of the ~500 kDa complex where ATAD3A was retrieved. To address this question, we generated ATAD3A mutants able to genetically distinguish the function of ATAD3A in the different

CellPress
OPEN ACCESS

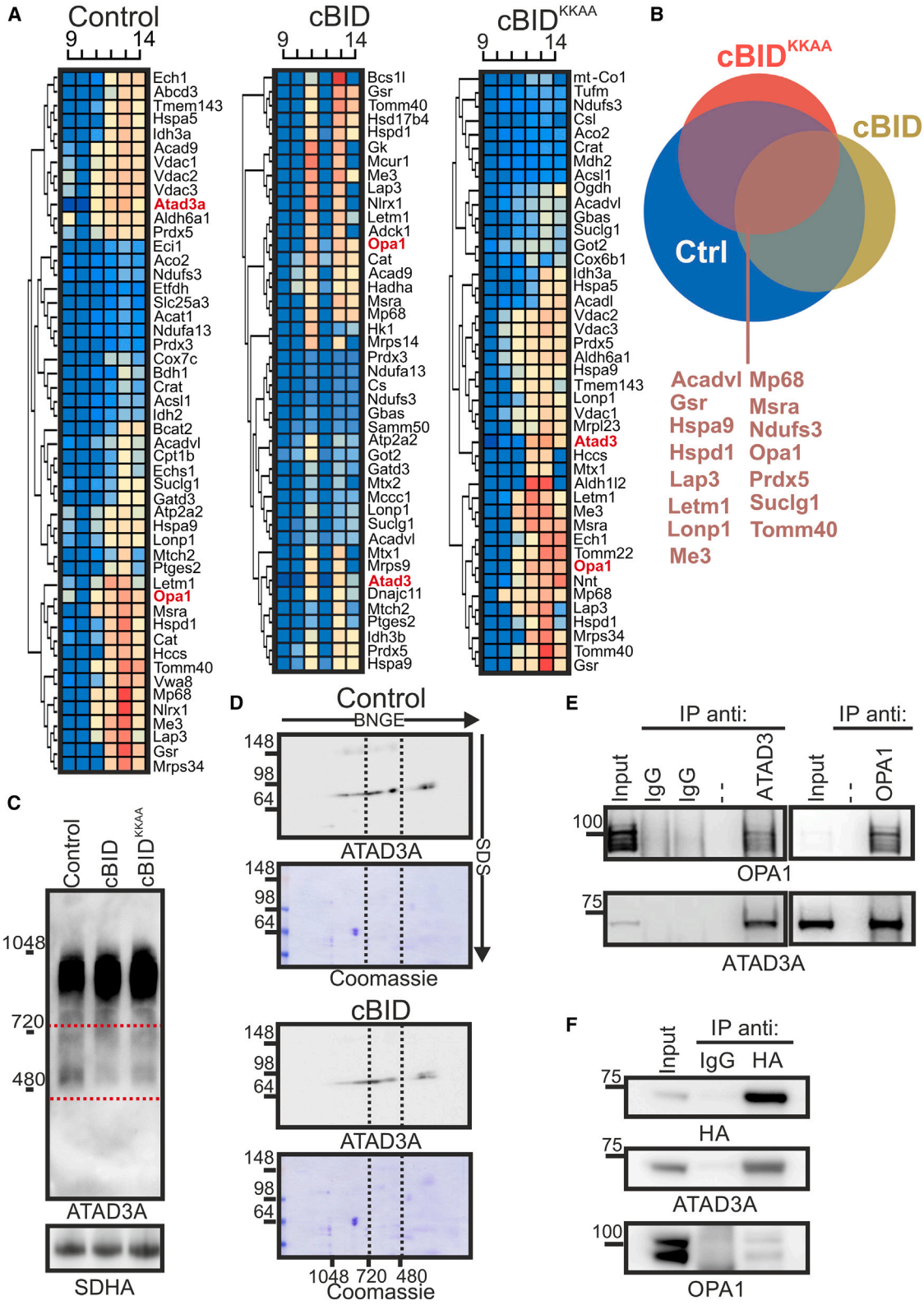

Figure 3. ATAD3A interactome analysis with MitoCIAO

(A) Heatmaps and hierarchical clustering of ATAD3A putative interactors at the *p* value $\leq$ 0.05 threshold in mouse heart mitochondria treated as indicated in the BNGE slices 9–14 as indicated above the heatmaps. The color scale indicates the normalized PSM distribution of each individual protein.

(legend continued on next page)

complexes where it was retrieved. Based on a homology model of ATAD3A, we generated three HA-tagged (at the C terminus), RNAi-resistant, different constructs of human ATAD3A isoform 2 (Q9NVI7-2): wild type (ATAD3A^{WT}-HA), an ATPase domain mutant in the Walker B site (ATAD3A^{ATPm}-HA), and a coiled-coil domain mutant (ATAD3A^{CCDm}-HA) (Figures S4A–S4C). Because all the constructs localized to mitochondria (Figure S4D), we proceeded to analyze their effect on cristae biogenesis. We first verified whether these mutants localized to different mitochondrial subcompartments. We silenced endogenous ATAD3A and expressed the RNAi-resistant WT as well as mutant ATAD3A together with a mitochondrially targeted monomeric dsRED (mtRFP) to identify cells re-expressing ATAD3A. By correlative light-electron microscopy (CLEM) combined with immunogold analysis in cells identified by their mtRFP, we observed that WT, as well as the ATAD3A mutants, were correctly targeted to the IMM. Of note, mitochondria re-expressing ATAD3A^{WT}-HA and ATAD3A^{CCDm}-HA possessed intact cristae, whereas these were completely absent in mitochondria from cells complemented by ATAD3A^{ATPm}-HA re-expression (Figure S4E).

The different cristae phenotype observed in cells reconstituted with ATAD3A^{CCDm} and ATAD3A^{ATPm} prompted us to investigate in detail whether cristae biogenesis required an intact ATAD3A ATPase domain. We confirmed that cristae density was reduced and CLW increased upon endogenous ATAD3A silencing. Re-expression of HA-tagged ATAD3A^{WT} or ATAD3A^{CCDm} but not of ATAD3A^{ATPm} restored cristae biogenesis and CLW (Figures 4A and 4C–4D). Silencing of ATAD3A also resulted in mitochondrial fragmentation that was rescued only by reintroduction of ATAD3A^{WT} (Figures 4B and 4E). These results indicate that ATAD3A requires a functional ATPase domain to participate in cristae biogenesis and both the ATPase and CC domains to maintain the mitochondrial network.

AAA+ ATPase family proteins exert their biological function as hexamers. We therefore investigated whether cristae biogenesis was similarly mediated by ATAD3A oligomerization, a process that depends on its coiled-coil domain.[32] To address this question, we investigated the impact of the studied ATAD3A mutations on its ability to oligomerize. We retrieved ATAD3A oligomers (stabilized by the chemical crosslinker EDC) in cells expressing the ATAD3A^{WT}-HA and ATAD3A^{ATPm}-HA, while in the cells expressing ATAD3A^{CCDm}-HA, the oligomers were very significantly reduced (Figures 4F and 4G), despite the fact that we did not observe major changes among the levels of the expressed ATAD proteins (Figure 4H). These results confirm that the coiled-coil domain is essential for ATAD3A dimerization. In total, our biochemical and electron microscopy (EM) analysis indicate that ATAD3A dimerization is not required to maintain mitochondrial ultrastructure.

The ~500 kDa ATAD3A complex participates in cristae morphology

Because our data indicate that only the ATPase domain of ATAD3A is essential for the maintenance of cristae morphology, we investigated whether the ATAD3A^{ATPm} was retrieved in the ~500 kDa OPA1-containing HMW complex that modulates cristae shape.[5] We therefore capitalized on the strategy of endogenous ATAD3A silencing followed by re-expression of small interfering RNA (siRNA)-resistant, HA-tagged ATAD3A WT and mutants. In BNGE experiments, ATAD3A^{WT} was retrieved in two distinct complexes at ~1 MDa and ~500 kDa. Conversely, ATAD3A^{CCDm} was found only in the ~500 kDa complex and ATAD3A^{ATPm} only in the ~1 MDa one. Interestingly, we retrieved less OPA1 in the ~500 kDa complex upon silencing of ATAD3A. Reintroduction of WT and CCDm, but not of the ATPm ATAD3A, corrected OPA1 assembly in these complexes (Figures 5A and 5B). Thus, ablation of ATAD3A reduced levels of OPA1 in the ~500 kDa complex that were corrected by the ATAD3A^{CCDm} mutant that can assemble in this complex. This differential assembly of OPA1 was not caused by a global reduction in its levels: while total OPA1 levels were reduced upon ATAD3A silencing, they were restored by reintroduction of all the mutants, including ATAD3A^{ATPm} that does not allow OPA1 assembly at ~500 kDa (Figures S5A and S5B). Analyses of mitochondrial respiratory control ratio (RCR), which is influenced by OPA1 oligomerization,[5] further confirmed the importance of ATAD3A for this function of OPA1. ATAD3A silencing indeed reduced RCR, and reintroduction of WT and ATAD3A^{CCDm}, but not of ATAD3A^{ATPm} that does not allow OPA1 assembly, restored it totally or partially, respectively (Figure S5C). To understand whether OPA1 was reciprocally required for ATAD3A assembly, we acutely ablated *Opa1* by adenovirus delivery of Cre to *Opa1*$^{flx/flx}$ MAFs.[5] Efficient *Opa1* deletion did not reduce total ATAD3A levels (Figure 5C) or impaired the ability of ATAD3A to oligomerize (Figure 5D). To measure whether *Opa1* deletion affected ATAD3A assembly in HMW complexes, we performed 2D BN-SDS-PAGE that allows efficient visualization of the different ATAD3A- and OPA1-containing complexes by immunoblotting. Because of the increased resolution of this 2D approach, we could further resolve the ATAD3A- and OPA1-containing complexes that are difficult to separate in single-dimension BN-PAGE. In control mitochondria, ATAD3A was retrieved in four main complexes. Similarly, OPA1 immunoreactivity was found in three main complexes. Between 480 and 720 kDa, we identified two complexes where OPA1 and ATAD3A comigrate, one immediately below 720 kDa and the second weakly immunoreactive for ATAD3A at approximately 550 kDa. Of note, deletion of OPA1 resulted in the disappearance of ATAD3A immunoreactivity at the 720 complex and in increased ATAD3A

(B) Venn diagram of the proteins identified as putative interactors of ATAD3A in experiments as in (A). The gene names of the putative ATAD3A interactors retrieved in the indicated Venn diagram intersection are indicated.
(C) Mouse heart mitochondria were treated as indicated, lysed, and equal amounts of proteins were separated by BNGE and immunoblotted using the indicated antibodies (representative western blot from $n = 3$ biological replicates). The dotted box highlights the ~500 kDa complex.
(D) Mouse heart mitochondria were treated as indicated, lysed, and equal amounts of proteins were separated by a 2D BN-SDS-PAGE and immunoblotted for ATAD3A or stained by Coomassie blue (representative from $n = 3$ biological replicates). The dotted box highlights the ~500 kDa complex.
(E and F) Mouse heart mitochondria (E) or MAFs transfected with ATAD3A^{WT}-HA (F) were lysed, and proteins were immunoprecipitated using the indicated antibodies, separated by SDS-PAGE, and immunoblotted using the indicated antibodies (representative from $n = 3$ biological replicates). The input is 1:5 of the total protein used for the IP.

CellPress
OPEN ACCESS

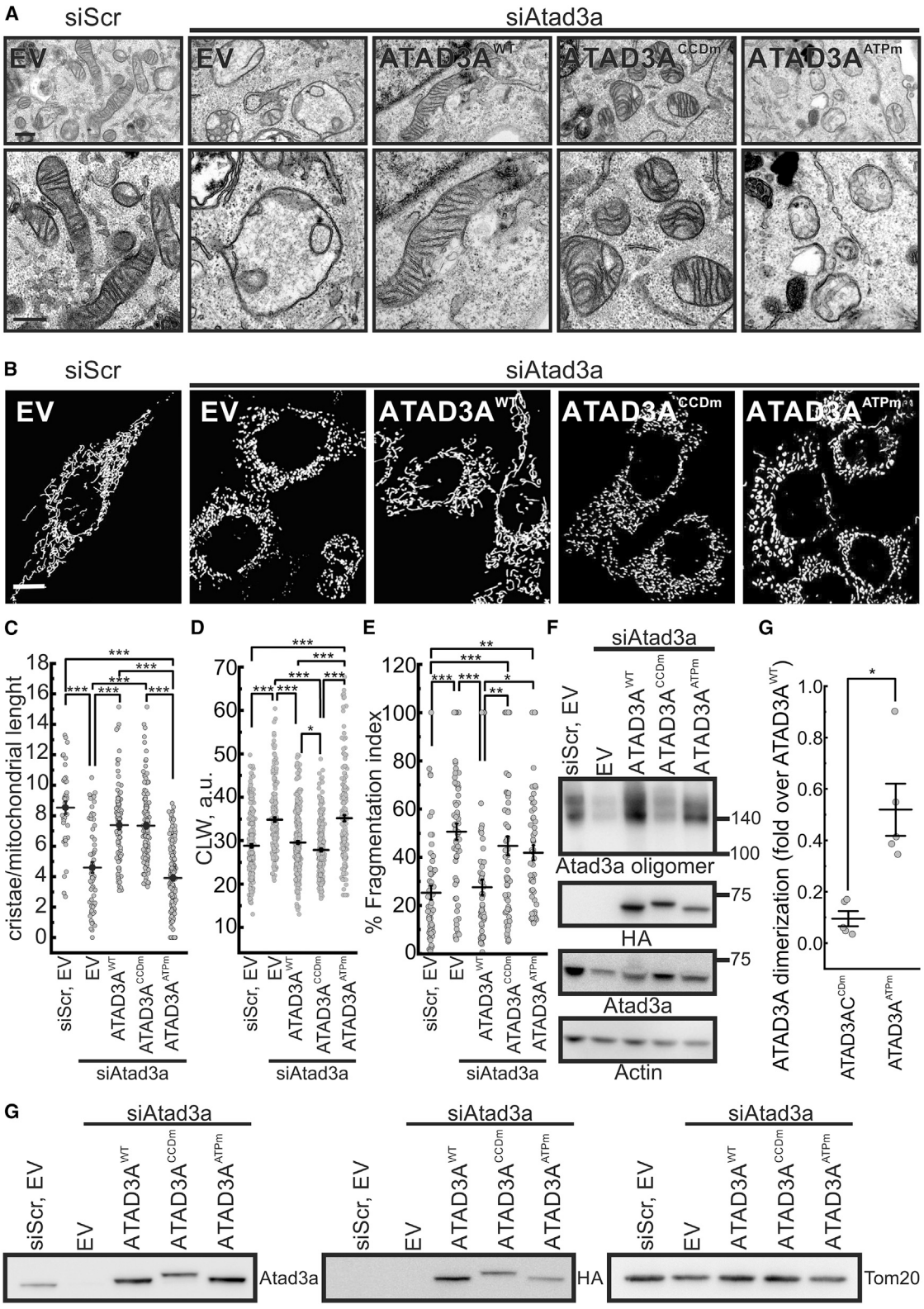

Figure 4. A functional ATPase domain of ATAD3A is required for cristae biogenesis

(A) Representative electron micrographs of CLEM in mtRFP^{+} MAFs cotransfected with the indicated siRNA, mtRFP, and the indicated plasmid (from n = 4 biological replicates). Scale bars: 1 μm (upper), 500 nm (lower).

(legend continued on next page)

immunoreactivity at 1,048 kDa (Figure 5E). This 2D approach thus identifies a specific ATAD3A and OPA1-containing complex that depends on OPA1 presence.

Because we were surprised to observe that assembly of OPA1 in a complex crucial for cristae biogenesis required ATAD3A, we decided to complete the epistatic analysis of the relative role of OPA1 and ATAD3A in the control of cristae shape. In *Opa1*$^{-/-}$ MEFs, reintroduction of OPA1 corrected the fragmented mitochondrial morphology and cristae biogenesis. Overexpression of ATAD3A in *Opa1*-deficient cells did not phenocopy the mitochondrial elongation observed upon OPA1 reintroduction but partially restored number and tightness of cristae. Coexpression of ATAD3A with OPA1 did not increase the effects observed upon OPA1 expression on mitochondrial morphology and cristae shape (Figures S6A–S6E). We next addressed whether amelioration of cristae shape by ATAD3A required the ATPase and the CCD domains. We silenced endogenous ATAD3A in Opa1$^{-/-}$ MEFs followed by re-expression of the ATAD3A CCD and ATPase mutants at comparable levels (Figure S6F). The partial cristae shape amelioration occurred only when ATAD3A^{WT} and ATAD3A^{CCDm} but not when ATAD3A^{ATPm} was expressed (Figure S6G). This analysis indicates that ATAD3A requires a functional ATPase domain to partially restore cristae shape even in the absence of OPA1. Because the ATAD3A^{CCDm} assembles only in the ~500 kDa complex containing OPA1, whereas ATAD3A^{ATPm} assembles only in the ~1 MDa complex, our data indicate that the ~500 kDa complex participates in cristae biogenesis and stability.

The ~1 MDa ATAD3A complex regulates mitoribosome stability

We used this same approach to deorphanize the function of the ~1 MDa complex that contains ATAD3A. We returned to MitoCIAO and inspected the potential partners of ATAD3A in the ~1 MDa complexes (slices 3–8) in unperturbed mitochondria. We identified several ATP synthase subunits as well as mitoribosomal proteins and proposed nucleoid interactors such as prohibitins (PHBs) (Figure S7A).[33,34] Our attention was caught by these mitoribosomal and nucleoid-associated proteins because of their proposed interaction.[34,35] Indeed, MARIGOLD confirmed that 33 mitoribosomal proteins (MRPL4, 9, 13, 15, 17, 18, 20, 21, 22, 23, 24, 27, 28, 34, 37, 38, 39, 41, 43, 44, 45, 49, and 50; MRPS 2, 5, 9, 14, 16, 21, 22, 23, 27, 30, 34, and 35) and the proposed nucleoid-interacting PHBs were retrieved in the ~1 MDa complex (Figures 6A and S7B). These data suggested that this complex comprises proteins involved in the regulation of mitochondrial nucleoids and/or mitoribosome stability. We therefore first analyzed whether lack of mitochondrial DNA (mtDNA) affected the ~1 MDa ATAD3A complex by MS analysis of BNGE-separated complexes in wt and ρ^0 cells where mtDNA was depleted by continuous exposure to ethidium bromide. In ρ^0 mitochondria we could not retrieve ATAD3A at ~1 MDa, supporting that ATAD3A assembles in this HMW region only when mtDNA is present (Figure S7C).

Because this experiment suggested a crosstalk between ATAD3A and nucleoids where mtDNA is packaged, replicated, and transcribed, we used the system of endogenous ATAD3A silencing with reintroduction of WT and mutant ATAD3A to address how nucleoid and mtDNA copy number were affected by ATAD3A levels and function. Imaging of picogreen-labeled mtDNA indicated a reduction in nucleoids in cells lacking endogenous ATAD3A and expressing ATAD3A^{CCDm} but not ATAD3A^{WT} and ATAD3A^{ATPm} (Figures 6B and 6C). This reduction was not caused by changes in mtDNA copy number (Figure 6D). These experiments support a role for the ~1 MDa complex of ATAD3A, where ATAD3A^{ATPm} assembles in nucleoid organization.

Nucleoids where mtDNA is replicated and transcribed spatially overlap and are often copurified by biochemical approaches with mitochondrial granules where translation occurs. We therefore tested whether the observed differences in nucleoid number could result from the potential association of ATAD3A with mitoribosomal proteins. To address this question, we first investigated by coIP experiments whether ATAD3A interacted with the mitoribosome machinery. Indeed, MRPS22 and MRPL13 coimmunoprecipitated with ATAD3A (Figure 6E). Moreover, levels of the mitoribosomal proteins MRPS22 and MRPL13 were reduced upon ATAD3A silencing and when these silenced cells were complemented with ATAD3A^{CCDm}, which does not assemble at ~1 MDa and does not restore nucleoid number (Figure S7D).

These results prompted us to investigate whether ATAD3A was required for the integrity of mitoribosome complex. Normally, in sucrose gradient sedimentation analyses, proteins of large (MRPL) and small (MRPS) mitoribosomal subunits are retrieved together in the high-density fractions, the expected location of the assembled mitoribosome. ATAD3A, but not other mitochondrial proteins such as VDAC or OPA1, was also found in the same fraction. Silencing of ATAD3A decreased MRPL13 and MRPS22 levels in this high-density fraction, an effect that was

(B) Representative volume-rendered 3D reconstructions of stacks of confocal images of mtRFP from $n = 3$ biological replicates of experiments as in (A). Scale bar: 10 μm.

(C and D) Quantification of number of cristae per μm mitochondrial length (C, 70–150 mitochondria per condition) and cristae lumen width (CLW, D, 200–350 cristae per condition) from 4 independent biological replicates as in (A) ($n = 25$–75 cells per condition). Dots represent individual measurements. Average ± SEM is plotted. $^{***}p \leq 0.001$; $p \leq 0.05$ in a one-way ANOVA with Tukey multiple pairwise comparisons.

(E) Mitochondrial fragmentation index from 3 independent biological replicates as in (B) ($n = 60$–65 cells per condition). Dots represent individual measurements. Average ± SEM is plotted. $^{***}p < 0.001$; $^{**}p \leq 0.01$; $^{*}p \leq 0.05$ in a one-way ANOVA with Tukey multiple pairwise comparisons.

(F) MAFs were transfected with the indicated siRNA and plasmids and crosslinked with EDC, and lysed and equal amounts of proteins were separated by SDS-PAGE and immunoblotted using the indicated antibodies (representative from $n = 4$–5 biological replicates).

(G) ATAD3A dimer/monomer ratio in $n = 4$–5 biological replicates of experiments as in (F) normalized to the ratio in cells expressing ATAD3A^{WT} and calculated by densitometry of the anti-HA bands. Dots represent individual measurements. Average ± SEM is plotted. $^{*}p \leq 0.05$ in a one-way ANOVA with Tukey multiple pairwise comparisons.

(H) MAFs cotransfected with the indicated siRNA, mtRFP, and the indicated plasmids as in (A) were lysed, and equal amounts of proteins were separated by SDS-PAGE and immunoblotted using the indicated antibodies (representative from $n = 5$ biological replicates).

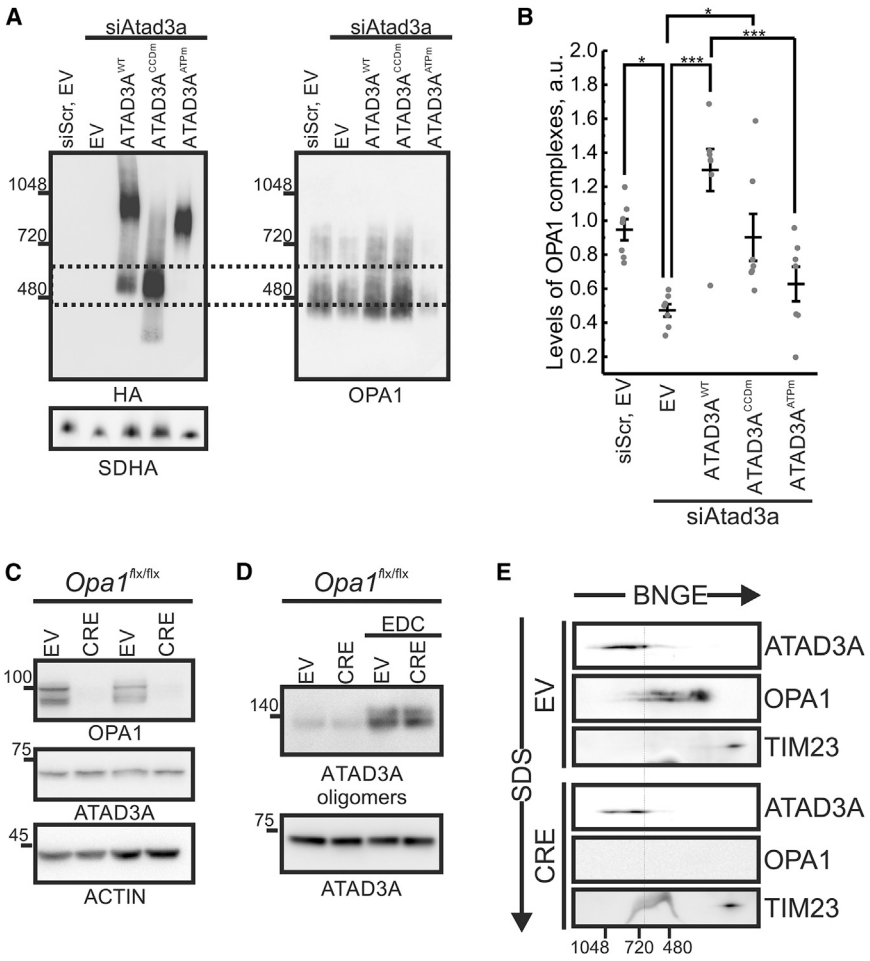

Figure 5. The ATAD3A ~500 kDa complex participates in cristae morphology

(A) MAFs were treated with the indicated siRNA, transduced with the indicated retroviruses, lysed, and equal amounts of proteins were separated by BNGE and immunoblotted using the indicated antibodies. The dotted box highlights the ~500 kDa complex (representative from $n = 7$ biological replicates).

(B) Densitometric analysis of SDHA-normalized OPA1 complexes levels in $n = 7$ biological replicates of experiments as in (A). Dots represent individual measurements. Average ± SEM is plotted. $^{***}p < 0.001$; $^{*}p \leq 0.05$ in a one-way ANOVA with Tukey multiple pairwise comparisons.

(C and D) *Opa1*$^{flx/flx}$ MAFs transduced with the indicated adenoviruses were lysed, and equal amounts of proteins were separated by SDS-PAGE and immunoblotted using indicated antibodies (representative from $n = 3$ biological replicates). In (D), where indicated cells were crosslinked with EDC.

(E) Mitochondria isolated from *Opa1*$^{flx/flx}$ MAFs transduced as indicated were lysed, and equal amounts of proteins were separated by a 2D BN-SDS-PAGE and immunoblotted with the indicated antibodies (representative from $n = 3$ biological replicates). The dotted line highlights a complex that disappears in *Opa1*$^{flx/flx}$ MAFs transduced with CRE adenoviruses.

rescued by expression of the ATAD3A^{WT} or ATAD3A^{ATPm}, but not ATAD3A^{CCDm}. Interestingly, when we rescued the silenced cells with ATAD3A^{CCDm}, we retrieved more ATAD3A in the fractions where OPA1 was also found (Figures 6F and S7E). Altogether, these data indicate that the ~1 MDa complex of ATAD3A is involved in mitoribosome stability.

DISCUSSION

Functionalization of the mitochondrial proteome provided unprecedented insights into mitochondrial function and involvement in disease. However, a major challenge is to deorphanize mitochondrial complexes with elusive composition that often execute the pleiotropic functions of mitochondrial proteins. Here, we provide two online, available, and searchable compendia of protein distribution in complexes extracted from native gels (MARIGOLD) and of the likelihood of protein-protein comigration in HMW complexes (MitoCIAO) to solve these issues and advance the deorphanization of the function of mitochondrial protein complexes. By validating the predictive power of these tools against the function of two elusive complexes comprising the mitochondrial protein ATAD3A, we genetically dissect how the same protein operates in cristae morphology and in the stability of mitochondrial ribosomes.

Databases of the mitochondrial proteome constitute a landmark tool for the discovery of molecules involved in mitochondrial function. They have been instrumental in discovering the molecular components of the mitochondrial Ca^{2+} uniport holoplex,[36] novel complex I subunits,[6] and the elusive mitochondrial pyruvate carrier.[37,38] Subsequently, proteomic databases of mitochondrial protein complexes ("complexomes") were developed and used to assign functions to previously uncharacterized complex I components or to discover novel MICOS components.[39,40] However, these databases do not provide insights into the dynamic nature of mitochondrial complexes and, more importantly, the likelihood that two proteins or sets of functionally similar proteins are retrieved in the same complex. The first information is essential given the very stable nature of most mitochondrial inner membrane proteins. Indeed, these proteins can persist undegraded for months,[9] raising the question of whether they engage in physiologically relevant interactions with multiple partners to fulfill their pleiotropic function across the months of their lifespan, when obviously mitochondrial and cellular physiology must change and adapt to the different environmental conditions. Knowing whether two proteins likely interact in a given HMW complex can help predict the function of orphan proteins and of HMW complexes. MARIGOLD and MitoCIAO close this gap and represent useful tools for discovering hitherto unappreciated functions of HMW complexes.

MARIGOLD represents an online tool for precision analysis of individual protein distribution in BNGE of mitochondrial samples

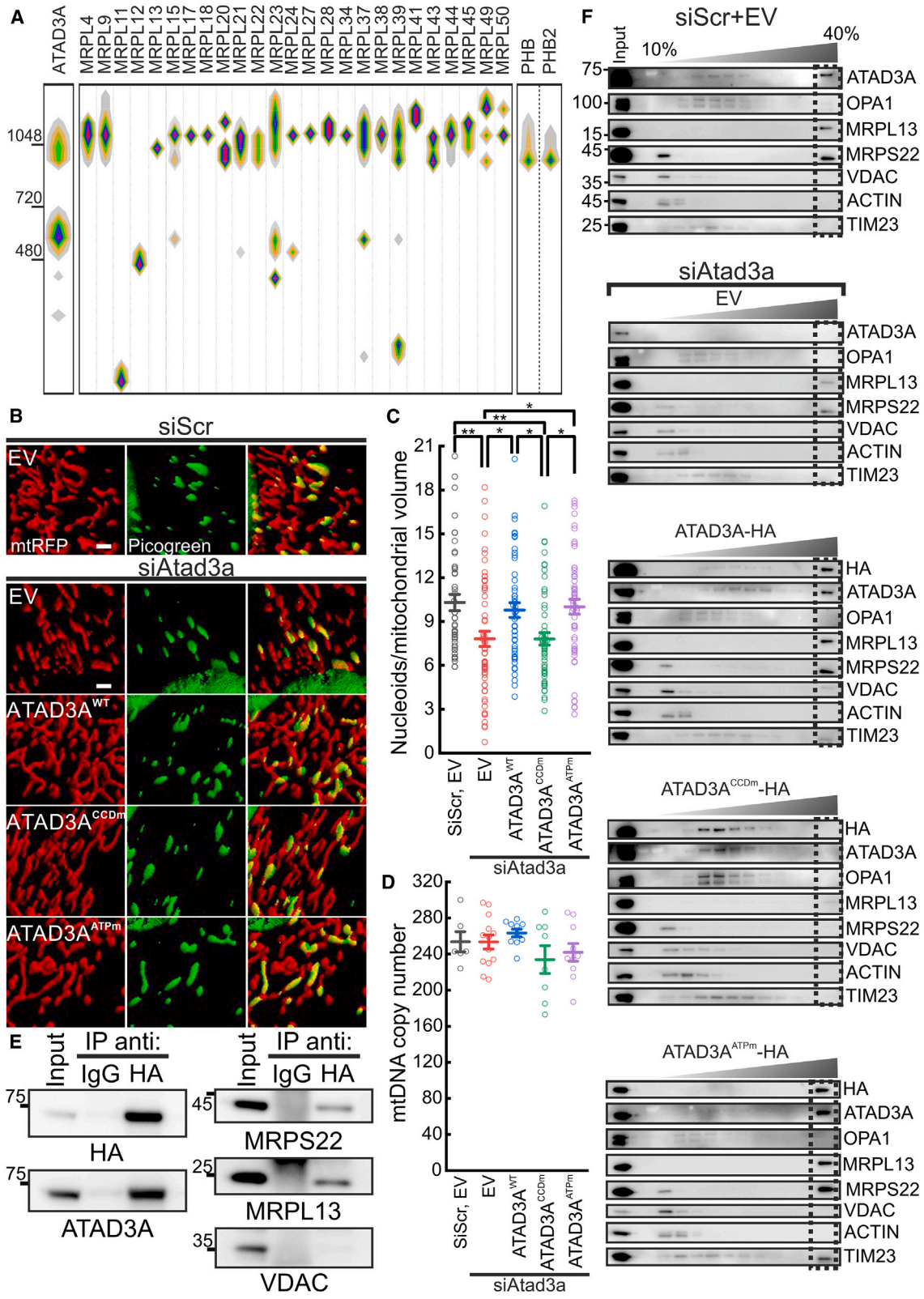

Figure 6. The ATAD3A 1 MDa complex regulates mitoribosome stability

(A) MARIGOLD color contour plots of BNGE distribution of ATAD3A, large subunit mitoribosomal proteins, and prohibitins (PHB and PHB2) in untreated mouse heart mitochondria.

(legend continued on next page)

dissolved in low digitonin concentrations that unlikely perturb complexes and supercomplexes. The contour plot visualization of the normalized PMS counts offers a more accurate account of protein distribution in BNGE than conventional immunoblotting and can be readily utilized. We foresee that MARIGOLD can bypass the common issue of poor antibody immunoreactivity against antigens, especially when non-denatured, rapidly becoming a golden standard for immediate, hands-free experiments of BNGE for a protein of interest. Furthermore, MARIGOLD can be used as a reference database to validate immunoreactivity of antibodies used in BNGE. MARIGOLD reports the distribution of the searched protein not only in unperturbed mitochondria but also in mitochondria undergoing MOMP and cristae remodeling or MOMP alone. This layer of complexity added to the database, without complicating its use by the community, serves two different purposes. First, it allows addressing the changes occurring at the mitochondrial level during the key process of apoptotic outer membrane permeabilization. Most of the early studies concentrated on the proteomic detection of proteins released from mitochondria during MOMP.[41,42] Our databases conversely address the issue of mitochondrial apoptotic changes from the perspective of the organelle and constitute a useful resource to investigate how changes in HMW complexes participate in mitochondrial physiology and cell death. Second, it allows to identify the migration pattern of a protein of interest in different mitochondrial pathophysiological conditions. Because such a migration profile can be obtained and downloaded in publication-ready format without the need to perform wet lab experiments for approximately 660 mitochondrial proteins, we foresee that MARIGOLD can spearhead research on most mitochondrial pathways during remodeling and apoptosis.

MitoCIAO uses MARIGOLD and a Bayesian statistical method to predict the likelihood that proteins are retrieved in a complex stably (i.e., irrespective of MOMP or cristae remodeling) or in each of the conditions analyzed here. The predictive power of MitoCIAO has been validated against the MICOS complex, for which comprehensive wet lab studies of complex composition and protein-protein interaction exist,[43] and its usefulness tested to identify ATAD3A as an interactor of OPA1 and of mitoribosome proteins and to deorphanize the function of the two ∼500 kDa and ∼1 MDa complexes where ATAD3A was retrieved.

ATAD3A silencing alters cristae morphology, but the molecular mechanisms underlying this effect were unclear.[31] Our data indicate that this function can be ascribed to the ∼500 kDa complex that contains OPA1 and ATAD3A only when the ATPase domain of the latter is intact. In mitochondria where the ATAD3A ∼500 kDa complex is not formed, OPA1 does not proficiently assemble in this HMW. Reciprocally, in OPA1-lacking mitochondria, ATAD3A is absent from the ∼500 kDa complex, and cristae morphology cannot be recovered, indicating that both proteins participate in cristae biogenesis via this specific complex. In conclusion, we show that both ATAD3A and OPA1 must assemble in the ∼500 kDa complex for cristae biogenesis and maintenance and that the formation of this complex requires the ATPase domain of ATAD3A.

In addition to the ∼500 kDa complex, ATAD3A is retrieved in MARIGOLD also in a ∼1 MDa complex that is remarkably stable upon cristae remodeling. This stability suggests that it does not participate in the biogenesis of the IMM and calls for its functionalization. MitoCIAO was also useful in this occasion. The predicted high-confidence interactors of ATAD3A in this HMW complex comprised several mitoribosomal proteins, as also indicated by earlier studies.[34,35] Nevertheless, the functional role of ATAD3A in mitochondrial ribosome biology remained unclear. Because the ∼1 MDa complex requires an intact ATAD3A CCD domain, we could design experiments to address the specific relevance of this complex for mitochondrial ribosome stability. Indeed, in mitochondria expressing the ATAD3A CCD mutant that fails to assemble in the ∼1 MDa complex, mitoribosomal proteins are not retrieved in the high-density fraction corresponding to the mature ribosome. In conclusion, by using ATAD3A as an example, we substantiate that the approach described here using dynamic complexome analysis and the resulting MARIGOLD and MitoCIAO databases allows to functionalize specific mitochondrial complexes with an unprecedented resolution. We expect that the mitochondrial biology community can find MARIGOLD and MitoCIAO useful tools to understand the function of the different mitochondrial complexes.

Limitations of the study

While MARIGOLD and MitoCIAO provide insights into mitochondrial protein interactions, several limitations should be considered. Our study utilizes mouse heart mitochondria, which may not fully represent the diversity of mitochondrial complexes across different tissues or species. Blue-native gel electrophoresis might not resolve all protein complexes, particularly very large complexes, or transient or low-abundance ones.[40] Furthermore, our choice to utilize a low dose of digitonin resulted in the identification of more proteins compared with existing mitochondrial complexomes of murine hearts,[40] but fewer when compared with yeast[44] or HEK293 cells.[45] Additionally, while we validated several MitoCIAO's predictions experimentally or

(B) Stacks of confocal images of mtRFP (red) and of the DNA stain picogreen (green) were acquired in MAFs transfected as indicated. Representative volume-rendered 3D reconstructions from $n = 4$ biological replicates are shown. Scale bar: 1 μm.

(C) Nucleoid number per mitochondrial volume in 4 biological replicates of experiments as in (B). Average ± SEM is plotted. Dots indicate individual measurements ($n = 50–70$ cells per condition). $^{**}p < 0.01$; $^{*}p < 0.05$ in a one-way ANOVA with Tukey multiple pairwise comparisons.

(D) MAFs were transfected with the indicated siRNA and transduced with the indicated retroviruses. mtDNA copy number was determined by qPCR. Average ± SEM is plotted. Dots represent individual measurements ($n = 2$ technical replicates from 4 biological replicates per condition).

(E) MAFs stably expressing ATAD3A^{WT}-HA were lysed, and proteins were immunoprecipitated using the indicated antibodies, separated by SDS-PAGE, and immunoblotted using the indicated antibodies (representative from $n = 3$ biological replicates). The input is 1:5 of the total protein used for the IP.

(F) MAFs were transfected with the indicated siRNA and transduced with the indicated retroviruses, lysed, and equal amounts of proteins were separated by sucrose gradients. The 23 fractions were collected, and equal amounts of proteins from the odd fractions 1 to 21 were separated by SDS-PAGE and immunoblotted using the indicated antibodies (representative from $n = 3$ biological replicates). The dotted box highlights the fraction containing the assembled mitoribosome.

by literature searches, it is uncertain whether its predictive ability holds true across the entire mitochondrial proteome.

RESOURCE AVAILABILITY

Lead contact

Requests for further information and resources should be directed to and will be fulfilled by the lead contact, Maria Eugenia Soriano, (mariaeugenia.soriano@unipd.it).

Materials availability

All unique reagents generated in this study are available from the lead contact with a completed materials transfer agreement.

Data and code availability

- The software required for identifying correlated PSM profiles among different proteins was implemented as a package for the R statistical system. The full source code is available on GitHub at the following repository: https://github.com/sales-lab/MitoCIAOData.
- The mass spectrometry proteomics data have been deposited to the ProteomeXchange Consortium via the PRIDE[46] partner repository with the dataset identifier PXD034828.
- Original, uncropped blots as well as individual measurements used to generate graphs are available in Data S1—source Data.
- Any additional information required to reanalyze the data reported in this paper is available from the lead contact upon request.

ACKNOWLEDGMENTS

This work was supported by Associazione Italiana per la Ricerca sul Cancro (AIRC) IG19991; European Research Council (ERC) FP7-282280 and European Union FP7 CIG PCIG13-GA-2013-618697; Fondazione Cariparo Progetto d'eccellenza SIGMI; Ministero dell'Università e della Ricerca (MUR) FIRB RBAP11Z3YA_005, PRIN 2017BF3PXZ; the National Recovery and Resilience Plan (NRRP), Mission 4, Component 2, Investment 1.4, funded by the European Union—NextGenerationEU; and Telethon GGP15091 (to L. Scorrano). Additional support was provided by Telethon GJC22073, M.U.R. PRIN 2022PLZP9T and 2022XL4TE9, and University of Padua DiBio PRID 2018 (to M.E.S.); AMED-CREST (grant number JP22gm1110006 to N.I.); Fondazione IRP Città della Speranza (to L. Salviati); and the Spanish Ministry of Science, Innovation, and Universities (PGC2018-097019-B-I00), the Instituto de Salud Carlos III (Fondo de Investigación Sanitaria grant PRB3) (PT17/0019/0003-ISCIII-SGEFI/ERDF, ProteoRed), and Foundation "La Caixa" (HR17-00247) (to J.V.). M.C.A. and C.G. were supported by a PhD fellowship for international PhD students from Fondazione Cariparo. M.N. was supported by a JSPS Postdoctoral Fellowship for abroad.

AUTHOR CONTRIBUTIONS

Conceptualization: G.R., E.C., C.G., J.A.E., L. Scorrano, and M.E.S.; investigation: G.R., E.C., C.G., M.C.-A., M.N., F.C., C. Rampazzo, M.S., and C.Q.; methodology: E.C., N.M., F.B., J.V., C. Romualdi, and G.S.; softwares & web tool: E.C., J.V., C. Romualdi, and G.S.; visualization: G.R., E.C., C.G., M.C.-A., L. Scorrano, and M.E.S.; writing–original draft: G.R., M.E.S., and L. Scorrano; funding acquisition: M.E.S. and L. Scorrano; resources: M.S., T.I., L. Salviati, S.M., and N.I.; supervision: M.E.S. and L. Scorrano.

DECLARATION OF INTERESTS

The authors declare no competing interests.

STAR★METHODS

Detailed methods are provided in the online version of this paper and include the following:

SUPPLEMENTAL INFORMATION

Supplemental information can be found online at https://doi.org/10.1016/j.cmet.2025.01.017.

Received: July 15, 2022
Revised: October 15, 2024
Accepted: January 20, 2025
Published: February 24, 2025

REFERENCES

1. Hackenbrock, C.R. (1966). Ultrastructural bases for metabolically linked mechanical activity in mitochondria. I. Reversible ultrastructural changes with change in metabolic steady state in isolated liver mitochondria. J. Cell Biol. *30*, 269–297.
2. Scorrano, L., Ashiya, M., Buttle, K., Weiler, S., Oakes, S.A., Mannella, C.A., and Korsmeyer, S.J. (2002). A distinct pathway remodels mitochondrial cristae and mobilizes cytochrome c during apoptosis. Dev. Cell *2*, 55–67.
3. Frank, S., Gaume, B., Bergmann-Leitner, E.S., Leitner, W.W., Robert, E.G., Catez, F., Smith, C.L., and Youle, R.J. (2001). The role of dynamin-related protein 1, a mediator of mitochondrial fission, in apoptosis. Dev. Cell *1*, 515–525.
4. Giacomello, M., Pyakurel, A., Glytsou, C., and Scorrano, L. (2020). The cell biology of mitochondrial membrane dynamics. Nat. Rev. Mol. Cell Biol. *21*, 204–224. https://doi.org/10.1038/s41580-020-0210-7.
5. Cogliati, S., Frezza, C., Soriano, M.E., Varanita, T., Quintana-Cabrera, R., Corrado, M., Cipolat, S., Costa, V., Casarin, A., Gomes, L.C., et al. (2013). Mitochondrial cristae shape determines respiratory chain supercomplexes assembly and respiratory efficiency. Cell *155*, 160–171. https://doi.org/10.1016/j.cell.2013.08.032.
6. Pagliarini, D.J., Calvo, S.E., Chang, B., Sheth, S.A., Vafai, S.B., Ong, S.E., Walford, G.A., Sugiana, C., Boneh, A., Chen, W.K., et al. (2008). A mitochondrial protein compendium elucidates complex I disease biology. Cell *134*, 112–123.
7. Rath, S., Sharma, R., Gupta, R., Ast, T., Chan, C., Durham, T.J., Goodman, R.P., Grabarek, Z., Haas, M.E., Hung, W.H.W., et al. (2021). MitoCarta3.0: an updated mitochondrial proteome now with sub-organelle localization and pathway annotations. Nucleic Acids Res. *49*, D1541–D1547. https://doi.org/10.1093/nar/gkaa1011.

8. Morgenstern, M., Peikert, C.D., Lübbert, P., Suppanz, I., Klemm, C., Alka, O., Steiert, C., Naumenko, N., Schendzielorz, A., Melchionda, L., et al. (2021). Quantitative high-confidence human mitochondrial proteome and its dynamics in cellular context. Cell Metab. *33*, 2464–2483.e18. https://doi.org/10.1016/j.cmet.2021.11.001.

9. Bomba-Warczak, E., Edassery, S.L., Hark, T.J., and Savas, J.N. (2021). Long-lived mitochondrial cristae proteins in mouse heart and brain. J. Cell Biol. *220*, e202005193. https://doi.org/10.1083/jcb.202005193.

10. Guerrero-Castillo, S., van Strien, J., Brandt, U., and Arnold, S. (2021). Ablation of mitochondrial DNA results in widespread remodeling of the mitochondrial complexome. EMBO J. *40*, e108648. https://doi.org/10.15252/embj.2021108648.

11. Calvo, E., Cogliati, S., Hernansanz-Agustín, P., Loureiro-López, M., Guarás, A., Casuso, R.A., García-Marqués, F., Acín-Pérez, R., Martí-Mateos, Y., Silla-Castro, J.C., et al. (2020). Functional role of respiratory supercomplexes in mice: SCAF1 relevance and segmentation of the Qpool. Sci. Adv. *6*, eaba7509. https://doi.org/10.1126/sciadv.aba7509.

12. Kuwana, T., Mackey, M.R., Perkins, G., Ellisman, M.H., Latterich, M., Schneiter, R., Green, D.R., and Newmeyer, D.D. (2002). Bid, Bax, and lipids cooperate to form supramolecular openings in the outer mitochondrial membrane. Cell *111*, 331–342.

13. Antonsson, B., Montessuit, S., Sanchez, B., and Martinou, J.C. (2001). Bax is present as a high molecular weight oligomer/complex in the mitochondrial membrane of apoptotic cells. J. Biol. Chem. *276*, 11615–11623.

14. Frezza, C., Cipolat, S., Martins de Brito, O., Micaroni, M., Beznoussenko, G.V., Rudka, T., Bartoli, D., Polishuck, R.S., Danial, N.N., De Strooper, B., and Scorrano, L. (2006). OPA1 Controls Apoptotic Cristae Remodeling Independently from Mitochondrial Fusion. Cell *126*, 177–189.

15. Glytsou, C., Calvo, E., Cogliati, S., Mehrotra, A., Anastasia, I., Rigoni, G., Raimondi, A., Shintani, N., Loureiro, M., Vazquez, J., et al. (2016). Optic Atrophy 1 Is Epistatic to the Core MICOS Component MIC60 in Mitochondrial Cristae Shape Control. Cell Rep. *17*, 3024–3034. https://doi.org/10.1016/j.celrep.2016.11.049.

16. Quintana-Cabrera, R., Quirin, C., Glytsou, C., Corrado, M., Urbani, A., Pellattiero, A., Calvo, E., Vázquez, J., Enríquez, J.A., Gerle, C., et al. (2018). The cristae modulator Optic atrophy 1 requires mitochondrial ATP synthase oligomers to safeguard mitochondrial function. Nat. Commun. *9*, 3399. https://doi.org/10.1038/s41467-018-05655-x.

17. Landes, T., Emorine, L.J., Courilleau, D., Rojo, M., Belenguer, P., and Arnauné-Pelloquin, L. (2010). The BH3-only Bnip3 binds to the dynamin Opa1 to promote mitochondrial fragmentation and apoptosis by distinct mechanisms. EMBO Rep. *11*, 459–465.

18. Chipuk, J.E., McStay, G.P., Bharti, A., Kuwana, T., Clarke, C.J., Siskind, L.J., Obeid, L.M., and Green, D.R. (2012). Sphingolipid metabolism cooperates with BAK and BAX to promote the mitochondrial pathway of apoptosis. Cell *148*, 988–1000. https://doi.org/10.1016/j.cell.2012.01.038.

19. Smith, A.C., and Robinson, A.J. (2016). MitoMiner v3.1, an update on the mitochondrial proteomics database. Nucleic Acids Res. *44*, D1258–D1261. https://doi.org/10.1093/nar/gkv1001.

20. Zerbes, R.M., Bohnert, M., Stroud, D.A., von der Malsburg, K., Kram, A., Oeljeklaus, S., Warscheid, B., Becker, T., Wiedemann, N., Veenhuis, M., et al. (2012). Role of MINOS in mitochondrial membrane architecture: cristae morphology and outer membrane interactions differentially depend on mitofilin domains. J. Mol. Biol. *422*, 183–191. https://doi.org/10.1016/j.jmb.2012.05.004.

21. Friedman, J.R., Mourier, A., Yamada, J., McCaffery, J.M., and Nunnari, J. (2015). MICOS coordinates with respiratory complexes and lipids to establish mitochondrial inner membrane architecture. eLife *4*, e07739. https://doi.org/10.7554/eLife.07739.

22. Anand, R., Strecker, V., Urbach, J., Wittig, I., and Reichert, A.S. (2016). Mic13 Is Essential for Formation of Crista Junctions in Mammalian Cells. PLoS One *11*, e0160258. https://doi.org/10.1371/journal.pone.0160258.

23. Guarani, V., McNeill, E.M., Paulo, J.A., Huttlin, E.L., Fröhlich, F., Gygi, S.P., Van Vactor, D., and Harper, J.W. (2015). QIL1 is a novel mitochondrial protein required for MICOS complex stability and cristae morphology. eLife *4*, e06265. https://doi.org/10.7554/eLife.06265.

24. Xie, J., Marusich, M.F., Souda, P., Whitelegge, J., and Capaldi, R.A. (2007). The mitochondrial inner membrane protein mitofilin exists as a complex with SAM50, metaxins 1 and 2, coiled-coil-helix coiled-coil-helix domain-containing protein 3 and 6 and DnaJC11. FEBS Lett. *581*, 3545–3549.

25. Bohnert, M., Zerbes, R.M., Davies, K.M., Mühleip, A.W., Rampelt, H., Horvath, S.E., Boenke, T., Kram, A., Perschil, I., Veenhuis, M., et al. (2015). Central role of Mic10 in the mitochondrial contact site and cristae organizing system. Cell Metab. *21*, 747–755. https://doi.org/10.1016/j.cmet.2015.04.007.

26. Zerbes, R.M., Höß, P., Pfanner, N., van der Laan, M., and Bohnert, M. (2016). Distinct Roles of Mic12 and Mic27 in the Mitochondrial Contact Site and Cristae Organizing System. J. Mol. Biol. *428*, 1485–1492. https://doi.org/10.1016/j.jmb.2016.02.031.

27. Huynen, M.A., Mühlmeister, M., Gotthardt, K., Guerrero-Castillo, S., and Brandt, U. (2016). Evolution and structural organization of the mitochondrial contact site (MICOS) complex and the mitochondrial intermembrane space bridging (MIB) complex. Biochim. Biophys. Acta *1863*, 91–101. https://doi.org/10.1016/j.bbamcr.2015.10.009.

28. Patten, D.A., Wong, J., Khacho, M., Soubannier, V., Mailloux, R.J., Pilon-Larose, K., MacLaurin, J.G., Park, D.S., McBride, H.M., Trinkle-Mulcahy, L., et al. (2014). OPA1-dependent cristae modulation is essential for cellular adaptation to metabolic demand. EMBO J. *33*, 2676–2691. https://doi.org/10.15252/embj.201488349.

29. Banerjee, S., and Chinthapalli, B. (2014). A proteomic screen with Drosophila Opa1-like identifies Hsc70-5/Mortalin as a regulator of mitochondrial morphology and cellular homeostasis. Int. J. Biochem. Cell Biol. *54*, 36–48.

30. Varanita, T., Soriano, M.E., Romanello, V., Zaglia, T., Quintana-Cabrera, R., Semenzato, M., Menabò, R., Costa, V., Civiletto, G., Pesce, P., et al. (2015). The OPA1-dependent mitochondrial cristae remodeling pathway controls atrophic, apoptotic, and ischemic tissue damage. Cell Metab. *21*, 834–844. https://doi.org/10.1016/j.cmet.2015.05.007.

31. Peralta, S., Goffart, S., Williams, S.L., Diaz, F., Garcia, S., Nissanka, N., Area-Gomez, E., Pohjoismäki, J., and Moraes, C.T. (2018). ATAD3 controls mitochondrial cristae structure in mouse muscle, influencing mtDNA replication and cholesterol levels. J. Cell Sci. *131*, jcs217075. https://doi.org/10.1242/jcs.217075.

32. Gilquin, B., Taillebourg, E., Cherradi, N., Hubstenberger, A., Gay, O., Merle, N., Assard, N., Fauvarque, M.O., Tomohiro, S., Kuge, O., and Baudier, J. (2010). The AAA+ ATPase ATAD3A controls mitochondrial dynamics at the interface of the inner and outer membranes. Mol. Cell. Biol. *30*, 1984–1996. https://doi.org/10.1128/mcb.00007-10.

33. Gerhold, J.M., Cansiz-Arda, Ş., Lõhmus, M., Engberg, O., Reyes, A., van Rennes, H., Sanz, A., Holt, I.J., Cooper, H.M., and Spelbrink, J.N. (2015). Human Mitochondrial DNA-Protein Complexes Attach to a Cholesterol-Rich Membrane Structure. Sci. Rep. *5*, 15292.

34. He, J., Cooper, H.M., Reyes, A., Di Re, M., Sembongi, H., Litwin, T.R., Gao, J., Neuman, K.C., Fearnley, I.M., Spinazzola, A., et al. (2012). Mitochondrial nucleoid interacting proteins support mitochondrial protein synthesis. Nucleic Acids Res. *40*, 6109–6121. https://doi.org/10.1093/nar/gks266.

35. Arguello, T., Peralta, S., Antonicka, H., Gaidosh, G., Diaz, F., Tu, Y.T., Garcia, S., Shiekhattar, R., Barrientos, A., and Moraes, C.T. (2021). ATAD3A has a scaffolding role regulating mitochondria inner membrane structure and protein assembly. Cell Rep. *37*, 110139. https://doi.org/10.1016/j.celrep.2021.110139.

36. Baughman, J.M., Perocchi, F., Girgis, H.S., Plovanich, M., Belcher-Timme, C.A., Sancak, Y., Bao, X.R., Strittmatter, L., Goldberger, O., Bogorad, R.L., et al. (2011). Integrative genomics identifies MCU as an essential component of the mitochondrial calcium uniporter. Nature *476*, 341–345.

37. Da Cruz, S., Xenarios, I., Langridge, J., Vilbois, F., Parone, P.A., and Martinou, J.C. (2003). Proteomic analysis of the mouse liver mitochondrial inner membrane. J. Biol. Chem. *278*, 41566–41571. https://doi.org/10.1074/jbc.M304940200.

38. Herzig, S., Raemy, E., Montessuit, S., Veuthey, J.L., Zamboni, N., Westermann, B., Kunji, E.R.S., and Martinou, J.C. (2012). Identification and functional expression of the mitochondrial pyruvate carrier. Science *337*, 93–96. https://doi.org/10.1126/science.1218530.

39. Weber, T.A., Koob, S., Heide, H., Wittig, I., Head, B., van der Bliek, A., Brandt, U., Mittelbronn, M., and Reichert, A.S. (2013). APOOL is a cardiolipin-binding constituent of the Mitofilin/MINOS protein complex determining cristae morphology in mammalian mitochondria. PLoS One *8*, e63683. https://doi.org/10.1371/journal.pone.0063683.

40. Heide, H., Bleier, L., Steger, M., Ackermann, J., Dröse, S., Schwamb, B., Zörnig, M., Reichert, A.S., Koch, I., Wittig, I., and Brandt, U. (2012). Complexome profiling identifies TMEM126B as a component of the mitochondrial complex I assembly complex. Cell Metab. *16*, 538–549. https://doi.org/10.1016/j.cmet.2012.08.009.

41. Patterson, S.D., Spahr, C.S., Daugas, E., Susin, S.A., Irinopoulou, T., Koehler, C., and Kroemer, G. (2000). Mass spectrometric identification of proteins released from mitochondria undergoing permeability transition. Cell Death Differ. *7*, 137–144. https://doi.org/10.1038/sj.cdd.4400640.

42. Van Loo, G., Demol, H., van Gurp, M., Hoorelbeke, B., Schotte, P., Beyaert, R., Zhivotovsky, B., Gevaert, K., Declercq, W., Vandekerckhove, J., and Vandenabeele, P. (2002). A matrix-assisted laser desorption ionization post-source decay (MALDI-PSD) analysis of proteins released from isolated liver mitochondria treated with recombinant truncated Bid. Cell Death Differ. *9*, 301–308. https://doi.org/10.1038/sj.cdd.4400966.

43. Kondadi, A.K., Anand, R., and Reichert, A.S. (2020). Cristae Membrane Dynamics - A Paradigm Change. Trends Cell Biol. *30*, 923–936. https://doi.org/10.1016/j.tcb.2020.08.008.

44. Schulte, U., den Brave, F., Haupt, A., Gupta, A., Song, J., Müller, C.S., Engelke, J., Mishra, S., Mårtensson, C., Ellenrieder, L., et al. (2023). Mitochondrial complexome reveals quality-control pathways of protein import. Nature *614*, 153–159. https://doi.org/10.1038/s41586-022-05641-w.

45. Wessels, H.J.C.T., Vogel, R.O., Lightowlers, R.N., Spelbrink, J.N., Rodenburg, R.J., van den Heuvel, L.P., van Gool, A.J., Gloerich, J., Smeitink, J.A.M., and Nijtmans, L.G. (2013). Analysis of 953 human proteins from a mitochondrial HEK293 fraction by complexome profiling. PLoS One *8*, e68340. https://doi.org/10.1371/journal.pone.0068340.

46. Perez-Riverol, Y., Bai, J., Bandla, C., García-Seisdedos, D., Hewapathirana, S., Kamatchinathan, S., Kundu, D.J., Prakash, A., Frericks-Zipper, A., Eisenacher, M., et al. (2022). The PRIDE database resources in 2022: a hub for mass spectrometry-based proteomics evidences. Nucleic Acids Res. *50*, D543–D552. https://doi.org/10.1093/nar/gkab1038.

47. Frangini, M., Franzolin, E., Chemello, F., Laveder, P., Romualdi, C., Bianchi, V., and Rampazzo, C. (2013). Synthesis of mitochondrial DNA precursors during myogenesis, an analysis in purified C2C12 myotubes. J. Biol. Chem. *288*, 5624–5635. https://doi.org/10.1074/jbc.M112.441147.

48. Vowinckel, J., Hartl, J., Butler, R., and Ralser, M. (2015). MitoLoc: A method for the simultaneous quantification of mitochondrial network morphology and membrane potential in single cells. Mitochondrion *24*, 77–86. https://doi.org/10.1016/j.mito.2015.07.001.

49. Acín-Pérez, R., Bayona-Bafaluy, M.P., Bueno, M., Machicado, C., Fernández-Silva, P., Pérez-Martos, A., Montoya, J., López-Pérez, M.J., Sancho, J., and Enríquez, J.A. (2003). An intragenic suppressor in the cytochrome c oxidase I gene of mouse mitochondrial DNA. Hum. Mol. Genet. *12*, 329–339. https://doi.org/10.1093/hmg/ddg021.

50. Cipolat, S., Martins de Brito, O., Dal Zilio, B., and Scorrano, L. (2004). OPA1 requires mitofusin 1 to promote mitochondrial fusion. Proc. Natl. Acad. Sci. USA *101*, 15927–15932. https://doi.org/10.1073/pnas.0407043101.

51. Frezza, C., Cipolat, S., and Scorrano, L. (2007). Organelle isolation: functional mitochondria from mouse liver, muscle and cultured fibroblasts. Nat. Protoc. *2*, 287–295. https://doi.org/10.1038/nprot.2006.478.

52. Schägger, H. (1995). Native electrophoresis for isolation of mitochondrial oxidative phosphorylation protein complexes. Methods Enzymol. *260*, 190–202.

53. Guarás, A., Perales-Clemente, E., Calvo, E., Acín-Pérez, R., Loureiro-Lopez, M., Pujol, C., Martínez-Carrascoso, I., Nuñez, E., García-Marqués, F., Rodríguez-Hernández, M.A., et al. (2016). The CoQH2/CoQ Ratio Serves as a Sensor of Respiratory Chain Efficiency. Cell Rep. *15*, 197–209. https://doi.org/10.1016/j.celrep.2016.03.009.

54. Varadi, M., Anyango, S., Deshpande, M., Nair, S., Natassia, C., Yordanova, G., Yuan, D., Stroe, O., Wood, G., Laydon, A., et al. (2022). AlphaFold Protein Structure Database: massively expanding the structural coverage of protein-sequence space with high-accuracy models. Nucleic Acids Res. *50*, D439–D444. https://doi.org/10.1093/nar/gkab1061.

55. Fukasawa, Y., Tsuji, J., Fu, S.C., Tomii, K., Horton, P., and Imai, K. (2015). MitoFates: improved prediction of mitochondrial targeting sequences and their cleavage sites. Mol. Cell. Proteomics *14*, 1113–1126. https://doi.org/10.1074/mcp.M114.043083.

56. Maier, J.A., Martinez, C., Kasavajhala, K., Wickstrom, L., Hauser, K.E., and Simmerling, C. (2015). ff14SB: Improving the Accuracy of Protein Side Chain and Backbone Parameters from ff99SB. J. Chem. Theor. Comput. *11*, 3696–3713. https://doi.org/10.1021/acs.jctc.5b00255.

STAR★METHODS

KEY RESOURCES TABLE

REAGENT or RESOURCE	SOURCE	IDENTIFIER
Antibodies		
ATAD3	Proteintech	Cat# 16610-1-AP; RRID: AB_2878288
OPA1	BD	Cat# 612607; RRID: AB_399889
Actin	Merck	Cat# MAB1501; RRID: AB_2223041
HA	SIGMA	Cat# H3663; RRID: AB_262051
TIM23	BD	Cat# 611223; RRID: AB_398755
TOM20	Santa Cruz	Cat# sc-11415; RRID: AB_2207533
VDAC1	Abcam	Cat# ab15895; RRID: AB_2214787
SDHA (Fp)	Abcam	Cat# ab14715; RRID: AB_301433
TFAM	Santa Cruz	Cat# sc-23588; RRID: AB_2303230
NDUFA9	Abcam	Cat# ab14713; RRID: AB_301431
mtCOX1	Abcam	Cat# ab14705; RRID: AB_2084810
ATP5A	Abcam	Cat# ab14748; RRID: AB_301447
MRPL13	Proteintech	Cat# 16241-1-AP; RRID: AB_2145705
MRPS22	Proteintech	Cat# 10984-1-AP; RRID: AB_2146488
HSP60	Santa Cruz	Cat# sc-13966; RRID: AB_2121457
GRP75	Santa Cruz	Cat# sc-13967; RRID: AB_647720
Caspase 3	Cell Signaling	Cat# 9661; RRID: AB_2341188
Sheep Anti-Mouse IgG HRP	GE healthcare	Cat#NA931; RRID: AB_772210
Donkey Anti-Rabbit IgG HRP	GE healthcare	Cat#NA934; RRID: AB_2722659
Rabbit Anti-Goat IgG HRP	Invitrogen	Cat# A27014; RRID: AB_2536079
Nanogold Fab GAR Ultra Small	Nanoprobes	Cat# 33C537; RRID: AB_3097757
Goat anti-Mouse IgG (H+L) Highly Cross-Adsorbed Secondary Antibody, Alexa Fluor 488	Thermo Fisher	Cat# A-11029; RRID: AB_2534088
Donkey anti-Rabbit IgG (H+L) Highly Cross-Adsorbed Secondary Antibody, Alexa Fluor 647	Thermo Fisher	Cat# A-31573; RRID: AB_2536183
Bacterial and Virus Strains		
Retroviral particles	This paper	N/A
Ad-CMV-GFP; Ad-CMV-Cre-GFP	Vector Biolabs	Cat# 1060; #1700
Chemicals, Peptides, and Recombinant Proteins		
Hygromycin	Invitrogen	Cat# 10687010
Polybrene	SIGMA	Cat# H9268
Polyethylenimine (PEI)	SIGMA	Cat# 408727
Picogreen	Life Technology	Cat# P7589
Saponin	SIGMA	Cat# 47036-50G-F
Digitonin	SIGMA	Cat# D141
GelCode Blue Stain	ThermoFisher	Cat# 24590
1-ethyl-3-(3-dimethylaminopropyl)carbodiimide hydrochloride (EDC)	Pierce	Cat# 22980
Triton-x-100	SIGMA	Cat# T8787
Uridine	SIGMA	Cat# U3003
Sodium Pyruvate	Gibco	Cat# 11360070
DMEM	SIGMA	Cat# D5796
Non-essential amino acids	SIGMA	Cat# M7145

(*Continued on next page*)

Continued

REAGENT or RESOURCE	SOURCE	IDENTIFIER
Fetal Bovine Serum	Gibco	Cat# 10500-064
Penicillin-Streptomycin	ThermoFisher	Cat# 15070063
HBBS	Gibco	Cat# 14025-050
ProLong Gold Antifade Mountant	Invitrogen	Cat# P36930
Goat Serum	SIGMA	Cat# G9023
Formaldehyde solution	SIGMA	Cat# 252549
Paraformaldehyde	SIGMA	Cat# P6148
Glutaraldehyde solution	EMS	Cat#16220
Epoxy embedding medium	SIGMA	Cat# 45345
GoldEnhance EM plus	Nanoprobes	Cat# 2114
N,N-dimethylacrylamide	SIGMA	Cat# 274135
β-mercaptoethanol	BioRad	Cat# 1610710
Bovine Serum Albumin	SIGMA	Cat# A6003
Bradford	SIGMA	Cat# B6916
Native Page Sample Buffer 4X	Invitrogen	Cat# BN2007
Native Page running buffer	Invitrogen	Cat# BN2001
Native Cathode buffer	Invitrogen	Cat# BN2002
NuPAGE MOPS	Invitrogen	Cat# NP0001
Trypsin	Promega	Cat# VA9000
Adenosine 5′-diphosphate sodium salt (ADP)	SIGMA	Cat# A5285
Oligomycin	SIGMA	Cat# O4876
2,4-Dinitrophenol (DNP)	SIGMA	Cat# D198501
ABT-737	APExBIO	Cat# A8193
Critical Commercial Assays		
DNeasy Blood and Tissue Kit	QIAGEN	Cat# 69506
Gold Enhancer EM	Nanoprobes	Cat# 2113
Human ACTB (Beta Actin) Endogenous Control (FAM™/MGB probe, non-primer limited)	Applied Biosystems	Cat# 4333762T
Taq Man Universal PCR Master Mix	Applied Biosystems	Cat# 4352341E
Precast Native 3-12% BisTris gels	Invitrogen	Cat# BN1001
Precast NuPAGE ZOOM 4-12% BisTris, IPG-well	Invitrogen	Cat# NP0330BOX
Precast NuPAGE 3-8% Tris-Acetate	Invitrogen	Cat# EA0375BOX
Precast NuPAGE 4-12% BisTris	Invitrogen	Cat# NP0321BOX
Deposited Data		
MitoCIAO Software	This paper	https://github.com/sales-lab/MitoCIAOData
Mass spectrometry proteomics data	This paper	ProteomeXchange Consortium via the PRIDE 46 partner repository; dataset identifier PXD034828
Original, uncropped blots	This paper	Data S1 - Source Data
Individual measurements used to generate graphs	This paper	Data S1 - Source Data
Experimental Models: Cell Lines		
ATAD3A-HA MAFs; ATAD3A^{CCDm}-HA MAFs; ATAD3A^{ATPm}-HA MAFs	This paper	N/A
Opa1$^{-/-}$::EV; *Opa1*$^{-/-}$::Opa1; *Opa1*$^{-/-}$::ATAD3A-HA	This paper	N/A
Platinum-E Retroviral Packaging (Plat-E)	Cell Biolabs	Cat# RV-10;1 RRID: CVCL_B488
Mouse wt and ρ^0 L929 cells	Laboratory of Prof. J.A. Enriquez.	N/A
Opa1$^{-/-}$ MEFs; *Opa1*$^{flx/flx}$ MAFs	Glytsou et al.[15]	N/A

(*Continued on next page*)

Continued

REAGENT or RESOURCE	SOURCE	IDENTIFIER
Oligonucleotides		
Stealth siRNA ATAD3A	Invitrogen	MSS272674
Stealth siRNA Negative control	Invitrogen	Cat# 12935300
mitochondrial cytochrome c oxidase subunit I TaqMan probe 6FAM-5-TACTACTAACAGACC-3-MGB	Applied Biosystems; custom probe Frangini et al.[47]	N/A
cytochrome c oxidase subunit I (forward) 5 -TGCTAGCCGCAGGCATTACT-3	Frangini et al.[47]	N/A
cytochrome c oxidase subunit I (reverse) 5-CGGGATCAAAGAAAGTTGTGTTT-3	Frangini et al.[47]	N/A
Recombinant DNA and proteins		
pCMV6-Kan/Neo-msAtad3a	OriGene	Cat# MC205186
pcDNA3.1(+)	ThermoFisher	Cat# V79020
pcDNA3.1(+)-amp-hATAD3A-HA	Laboratory of Prof. N. Ishihara	N/A
pcDNA3.1(+)-amp-hATAD3A^{CCDm}-HA	Laboratory of Prof. N. Ishihara	N/A
pcDNA3.1(+)-amp-hATAD3A^{ATPm}-HA	Laboratory of Prof. N. Ishihara	N/A
pMSCVhyg-EV	Takara	Cat# S1911
pMSCVhyg-hATAD3A-HA	This paper	N/A
pMSCVhyg-hATAD3A^{CCDm}-HA	This paper	N/A
pMSCVhyg-hATAD3A^{ATPm}-HA	This paper	N/A
Recombinant cBID or cBID^{KKAA}	Cogliati et al.[5]	N/A
Software and Algorithms		
ImageJ plugin MitoLoc	Vowinckel et al.[48]	http://www.gurdon.cam.ac.uk/stafflinks/downloadspublic/imaging-plugins
ImageJ	ImageJ	https://imagej.net
R	R Core Team	https://www.R-project.org
plumber	Barret Schloerke	https://www.rplumber.io/
React	Facebook Open Source	https://reactjs.org/
D3.js	Mike Bostock	https://d3js.org/
venn.js	Ben Frederickson	https://github.com/benfred/venn.js
STRING 11.0	String	http://string-db.org/
MitoMiner	Smith and Robinson[19]	http://mitominer.mrc-mbu.cam.ac.uk
MOE	Chemical Computing Grup (CCG)	www.chemcomp.com
MultAlin	Multalin	http://multalin.toulouse.inra.fr/multalin/
Other		
Dynabeads® Protein G for Immunoprecipitation	Thermo Fisher	Cat# 10004D
Anti-HA Magnetic Beads	Pierce	Cat# 88836; RRID: AB_2749815
Photoetched Cover Slips	Electron Microscopy Sciences	Cat# 102097-886

EXPERIMENTAL MODEL AND STUDY PARTICIPANT DETAILS

Animals

All mice procedures were performed according to approved protocols (protocol 32/2011 CEASA University of Padova and Venetian Institute of Molecular Medicine and protocol 564/2020 Italian Ministry of Health, University of Padova and Veneto Institute of Molecular Medicine). Three-four months old male C57BL6/J were maintained at a 12h light/dark cycle at a controlled room temperature range of 19-22°C. Mice were housed at a density of 3-4 per cage, with environmental enrichment and ad libitum access to drinking water and regular chow, checked daily by animal facility technicians and weekly by the University of Padova Veterinary Service for signs of distress. For organ harvesting, mice were anesthetized and euthanized according to the approved protocol.

Cell lines

Opa1$^{+/+}$ and Opa1$^{-/-}$ MEFs, *Opa1*$^{flx/flx}$ MAFs, were previously described[5] and their genotypes were periodically confirmed by PCR and western blot. The Platinum-E Retroviral Packaging (Plat-E) cells were kindly provided by Prof. Yassemi Capetanaki (BRFAA,

Greece). Cells were maintained in 5% CO_2 at 37°C in Dulbecco's modified Eagle's medium complete-high glucose (DMEM, Sigma; Cat. # D5796), 10% FBS (Gibco; Cat # 10500-064), 50 μg/ml Streptomycin-50 U/ml Penicillin (Invitrogen 15070063), non-essential amino acids (Sigma; Cat # M7145); 50 μg/ml Uridine (only in *Opa1*$^{-/-}$ MEFs; Sigma; Cat # U3003), 1mM Sodium Pyruvate (Gibco; Cat # 11360070). Mouse wt and ρ^0 L929 cells were previously generated[49] and grown in DMEM supplemented with 5% FBS, 50 μg/ml Uridine, and 1 mM sodium pyruvate.

METHOD DETAILS

Plasmids, oligos, and Transfection

The plasmid pCMV6-Kan/Neo-mouse Atad3a was purchased from OriGene (Cat. # MC205186) and sub-cloned in a pcDNA3.1(+) plasmid. The constructs with the human ATAD3A pcDNA3.1(+)-ATAD3A^{WT}-HA, pcDNA3.1(+)-ATAD3A^{CCDm}-HA, pcDNA3.1(+)-ATAD3^{ATPm}-HA were generated in Prof. N. Ishihara Laboratory. The ATAD3A^{CCDm}-HA has two mutations in each coiled-coil domain in the residues L93P, L103P, A193P, and A204P. The ATAD3A^{ATPm}-HA has the mutation E412Q in the Walker B site. The retroviral constructs pMSCVhyg-ATAD3A^{WT}-HA, pMSCVhyg- ATAD3A^{CCDm}-HA, pMSCVhyg- ATAD3^{ATPm}-HA were generated subcloning from the pcDNA3.1(+) constructs. pMSCV-Opa1 was used for Opa1 expression. Mitochondrially targeted red fluorescent protein (mtRFP) was previously described.[50] For ATAD3A silencing, Stealth ATAD3A siRNA was purchased from Invitrogen (Cat. # 1320001; siRNA ID: MSS272674).

For transfection, cells were seeded at a confluence of 60% in a 6-well plate. Silencing of ATAD3A was performed with 10 μl of 20 μM ATAD3 siRNA (Invitrogen; Cat. # 1320001) combined with 15 μg of PEI (Polysciences; Cat. # 24765) in 200 μl of incomplete DMEM. Negative Control siRNA (Ambion; Cat # AM4620) was used as control. After 20 minutes of incubation at RT, the solution was added directly to cells into 2 ml of complete DMEM. After 16 hours, the medium was replaced with fresh one, and cells were analyzed after 48-72h. For concomitant ATAD3A^{WT}-HA, ATAD3A^{CCDm}-HA or ATAD3A^{ATPm}-HA transient expression, cells at 50% confluence were incubated with siAtad3a oligos as indicated above, and the day after the cells were cotransfected with mt-RFP (0.5 μg) and the indicated plasmids (1.5 μg) combined with 15 μg of PEI. Cells were analyzed 48 h after plasmids cotransfection (72 h after silencing).

Retrovirus production and transduction

Virus particles were produced by transfecting 60% confluent Plat-E cells with 3 μg of one of the following plasmids pMSCVhyg-EV, pMSCVhyg-hATAD3A-HA, pMSCVhyg-hATAD3A^{CCDm}-HA or pMSCVhyg-hATAD3A^{ATPm}-HA. After 48h, the supernatant containing viral particles was collected, centrifuged (250 x *g*) and filtered (0.45 mm) to eliminate cell debris. Viral particles were then ultracentrifuged (31900 RPM, 2h) and pellets resuspended in PBS with 1% BSA. Titration was done to determine optimal viral concentration for transduction. For infection, Opa1$^{-/-}$ MEFs or wild-type MAFs were seeded at 60% confluence and the medium was supplemented with 10μg/ml of Polybrene (Hexadimethrine bromide, Sigma; Cat. #H9268). After 15 minutes, cells were infected with the optimal amounts of retroviral particles. After 24 h, the cell medium was replaced with DMEM, and the indicated analysis were performed after 48-72h. Where indicated, infection was performed 24h after silencing.

To induce *Opa1* ablation, *Opa1*$^{flx/flx}$ MAFs were infected with adenoviruses expressing cytomegalovirus (CMV)-Cre-GFP (ad-CRE; 450 pfu/cell; Vector Biolabs Cat. # 1700) or CMV-GFP (ad-EV, Vector Biolabs Cat. # 1060) as control, with the addition of Polybrene (4μg/μl). After 24h the medium was replaced with fresh one. After 72h, cells were collected and processed for SDS-PAGE, 2D BNGE-SDS-PAGE followed by western blot against the proteins indicated in the figure legends.

Mitochondrial isolation and in vitro cBID incubation

Mitochondria from C57BL/6 mice or MAFs were isolated as previously described.[51] Where indicated, mitochondria (1 mg/ml) were incubated in Experimental buffer (150mM KCl, 10mM Tris-MOPS, 5mM Pi, 20mM EGTA-Tris) containing complex I substrates (5mM Glutamate/ 2.5mM Malate) in the presence or absence of 40 pmol/mg of the recombinant proteins cBID or cBID^{KKAA}, 20 min at RT. Mitochondria were then centrifuged at 12000 x *g*, 10 min, 4°C, and pellets were processed for complexes extraction and BNGE and 2D BNGE-SDS-PAGE.

BNGE, 2D BNGE-SDS, and SDS-PAGE

Protein complexes extraction from isolated mitochondria (250 μg) was performed in 50 μl NativePage buffer 1X (NB, Invitrogen; Cat. # BN2003) with Proteases Inhibitor Cocktail (1:100) (PIC, Sigma; Cat. # P8340) and a 1.25% digitonin final concentration (Sigma; Cat. # D141). After 15 min in ice, samples were centrifuged at 17000 x *g*, 30min, 4°C; the supernatant (SN) was collected, and 1.8 μl of 5% Coomassie Brilliant Blue R-250 (Invitrogen; Cat. # BN20041) was added to the sample.

To extract mitochondrial complexes from cells, 2x10^6 cells were resuspended in 400 μl PBS containing 4mg/ml digitonin and incubated for 10 min in ice. After adding 1ml of cold PBS, samples were centrifuged at 9500 x *g*, 10 min, 4°C. The pellet was washed with PBS and resuspended in 100 μl NB with 1,25% digitonin. After 5 min in ice, mixture was centrifuged at 17000 x *g*, 30 min, 4°C. The SN was collected and 3.6 μll of 5% Coomassie Brilliant Blue R-250 was added.

For proteomic analysis of complexes extracted from isolated mitochondria, the samples were run in homemade 20 x 20 cm, 3-13% BNGE[52] (). Samples (200 μg) were separated in the presence of a dark blue Cathode buffer at 120 V, 4h, and then replaced with bright blue and run at 110V, O/N. The gel was stained with GelCode Blue Stain (Thermo Scientific, Cat #24590) before proceeding with

bands slicing and proteomics. The same bands from three independent experiments were pooled to compensate for biological variation between individuals.

For the other BNGE, protein complexes were separated in a Precast Native 3-12% BisTris gels (Invitrogen; Cat. # BN2011BX10). Samples were run in the presence of a dark blue Cathode buffer at 150 V, 45 min, then replaced with bright blue and ran at 250V, 90 min. Where indicated, protein complexes were transferred to a PVDF membrane O/N. The membrane was then treated with 8% acetic acid 5 min, washed with water, and let dry before proceeding with reactivation, blocking, and incubation with the indicated antibodies (ATAD3A, 1:1000, 2h; SDHA, 1:1000, 2h; OPA1, 1:1000, O/N; HA, 1:1000, 2h; GRP75, 1:2000, 2h; Secondary antibodies,1:3000, 1h).

To proceed with a second dimension SDS, the BNGE lane was excised and incubated for 15 min with each one of the following buffers in sequence: RSa (NuPAGE LDS sample buffer (Invitrogen; Cat # NP0007) with 4% b-mercaptoethanol); RSb (NuPAGE LDS sample buffer with 1% N,N-dimethylacrylamide (Sigma; Cat. # 274135); RSc (NuPAGE LDS sample buffer with 20% ethanol and 0,1% b-mercaptoethanol). After the last treatment, the lane was loaded in a 4-12% Bis-Tris ZOOM gel (Invitrogen; Cat. # NP0330BOX), run at 100V. Proteins were transferred to a PVDF membrane as indicated above, and immunodetection was done with the indicated antibodies. Where indicated the gel was stained with Coomassie blue. Gels for western blot and Coomassie were run in the same chamber in parallel for each experimental condition.

SDS-PAGE were performed with mitochondrial or cell lysates obtained after incubation in RIPA buffer, 30 min in ice. After centrifugation at 17000 x *g*, the SN was conserved and the protein quantified with Bradford reagent (Sigma Cat #B6916) by using a titration curve with BSA (Sigma, Cat #: A6003). LB sample buffer 2X or 4X (containing 5% b-mercaptoethanol as final concentration), was added to the SN. Samples were then boiled and loaded in NuPAGE Precast SDS-PAGE (Invitrogen).

Label-free proteomics analysis

For the proteomic analysis, mitochondria were isolated from three C57Bl/6 mice and independently treated or not with cBID or $cBID^{KKAA}$ as described above. Three different experiments for each experimental condition were loaded in parallel in a BNGE. After electrophoresis and gel staining as described above, each lane was excised in 25 bands covering the whole lane. Next, the same bands from the triplicate samples were pooled, minced, and digested with modified porcine trypsin (1:20) (Promega, Cat # VP9000) O/N in 100mM ammonium bicarbonate, pH 8.8, 37°C. The resulting tryptic peptide mixtures were subjected to nano-liquid chromatography coupled to mass spectrometry using a data-independent scanning (DiS) method as previously described.[52] Briefly, peptides were injected onto a C-18 reversed-phase nano-column (75 mm I.D and 50 cm, Acclaim PepMap100, Thermo Scientific) and analyzed in a continuous acetonitrile gradient consisting of 0-30% B in 240 min, 50-90% B in 3 min (B=90% acetonitrile, 0.5% acetic acid). A flow rate of ca. 200 nL/min was used to elute peptides from the RP nano-column to an emitter nanospray needle for real ionization and peptide fragmentation on an Orbitrap Fusion mass spectrometer (Thermo Fisher, San Josè, CA, USA).

Protein identification was made with Sequest running under Proteome Discover 1.4.0.288 (ThermoFisher), allowing two missed cleavages and using 3 Da and 20 ppm precursor and fragment mass tolerances, respectively. False discovery rate (FDR) of identification was controlled as described by the algorithm Dxtrator.[53]

MARIGOLD and MitoCIAO generation

After the mass spectrometry analysis, each identified protein had a score value for every spot analyzed; thus, for every hit, we obtained a pattern of identification along the whole electrophoretic run. The results were filtered for the mitochondrial predicted proteins using the proteomics database MitoMiner (http://mitominer.mrc-mbu.cam.ac.uk). Each remaining protein not identified by MitoMiner was manually checked for putative mitochondrial localization based on literature data. The strength of the relation between the identification patterns of each protein and a chosen reference protein was calculated using Spearman's rank correlation coefficient (ρ). The $\rho > 0$, and pairs of proteins with a negative correlation index ($\rho < 0$) have been removed from the subsequent analysis. Significant correlation can be selected from the web page (p-value $\geq$ 0.01 up to 0.1) and in this manuscript is indicated in the Figure's captions.

For staggered analysis, the electrophoretic run was divided into three regions: Bands 1-8, Bands 9-14, Bands 15-25. For the hierarchical clustering and the heatmap generation, the results were normalized to the sum of the spectral counts of a specific protein from all the spots in each selected region (1-8; 9-14; 15-25; or 1-25). All the analyses have been performed using R platform (https://www.R-project.org).

The MitoCIAO website has been developed as a two-tier application. The backend is implemented in the R language and uses the plumbr library to expose a REST API. The JavaScript fronted is organized as a single-page application (SPA) and builds on the React framework (https://reactjs.org/). Dendrograms are drawn using the D3 library (https://d3js.org/); Venn diagrams are plotted by venn.js (https://github.com/benfred/venn.js). Color contour plots were generated by using the DiS contour plot script in R [contour, graphics (version 3.6.2)], developed in J. Vazquez Laboratory.

Bioinformatic model

The mouse ATAD3A isoform 1 (UniProt: Q925I1) model was built using the homology modeling protocol implemented in the MOE suite (Molecular Operating Environment; https://www.chemcomp.com). A multiple template strategy was achieved by selecting the most appropriate template for different protein regions using Hidden Markov Model profiles (HMMs) comparison from HHpred[54] and de novo predicted model generated by AlphaFold[54] (entry: AF-Q925I1-F1). The first 34 amino acids were excluded from the model generation since identified as mitochondrial targeting sequence according to MitoFates server.[55] The entry 6B5C were

retrieved from the Protein Data Bank (www.pdb.it) for the ATPase domain (region 306-560; Probability: 99.72%, E-value: 2.4e-15, Score: 153.25, Identities: 21%). Despite the structure 6B5C was the 3rd entry according HHprep score, it was selected due to the highest resolution. This experimental structure prepared with the MOE structure preparation tool to add hydrogen atoms, fix missing atoms, and assign partial charges, and finally superposed. For the N-terminal region including the two coiled-coil regions and the trans membrane portion was obtained from de novo prediction from AlphaFold. The homology model was obtained by generating 10 different models using Amber12 Force Field[56] and selecting the best one according to the GB/VI score. The obtained model was further refined by ModRefiner.

Correlative light electron microscopy (CLEM) and TEM

Cells in the experimental conditions indicated were seeded in a 24 wells plate with a gridded coverslip (Electron Microscopy Sciences EMS; Cat. # 102097-886) at 20% confluence. Forty-eight hours after cotransfection with mtRFP and the indicated constructs, fluorescent and bright-field images were acquired at a Leica DMI4000B microscope to identify cotransfected cells and the coordinates in the gridded coverslips. After identifying the cells of interest, samples were processed for TEM and flat-embedded in resin. Briefly, samples were fixed with 2.5% glutaraldehyde (EMS; Cat. # 16220) in 0.1 M sodium cacodylate buffer pH 7.4 (freshly prepared) for 1 hour at 4°C, postfixed with a mixture of 1% osmium tetroxide and 1% potassium ferrocyanide in 0.1M sodium cacodylate buffer for 1 hour at 4°C. After three washes with water, samples were dehydrated in a graded ethanol series and embedded in an epoxy resin (Sigma; Cat. # 46345). Glass coverslips were removed with Hydrofluoric acid remaining the coordinates engraved onto the resin surface, thus allowing the cell tracking. Ultrathin sections (60-70 nm) were obtained with an Ultrotome V (LKB) ultramicrotome, counterstained with uranyl acetate and lead citrate, and viewed with a Tecnai G2 (FEI) transmission electron microscope operating at 100 kV. Images were captured with a Veleta (Olympus Soft Imaging System) digital camera. Images of the cells of interest identified with the aid of the grid were acquired and lately used for morphometric analysis.

Immunogold

Cells were fixed in a 24 wells plate with fresh 4% Paraformaldehyde (PFA; Sigma, Cat. # P6148) in PBS (pH 7,4) for 30 min, RT. The cells were then washed with PBS (5 x 5 min), incubated with blocking solution (0.5% bovine serum albumin (BSA), (Sigma; Cat. # A6003) 0.1% saponin, (Sigma; Cat. # 47036-50G-F) in PBS for 1h, RT. The primary antibody (ATAD3A: Proteintech 16610-1-AP; TOM: Santa Cruz, sc-11415; HA: Sigma,H3663) diluted 1:50 in blocking solution was incubated O/N, 4°C, to then proceed with several washes with PBS (5 min each). Cells were then incubated with the secondary antibody Nanogold Fab GAR Ultra Small (Nanoprobes; 1:100; Cat. # 33C537) for 4h, RT. After washing, cells were incubated with Gold Enhancer EM Plus (Nanoprobes; Cat. # 2114) by variable time to obtain proper staining conditions. After washing, cells were fixed with 2% glutaraldehyde in PBS for 30 min, RT, and then processed as described above for TEM analysis and imaging.

Mitochondrial morphometric analysis

TEM images were used to quantify cristae number per mitochondrial length and cristae lumen width (CLW) by using ImageJ (NIH). Length and cristae lumen width was quantified with the ImageJ Freehand line selection tool, while cristae number was manually quantified by two different operators blinded to the identity of the sample.

Confocal microscopy analysis

Cells cotransfected in the experimental conditions indicated in the figures were trypsinized and seeded in 6-well plates with glass coverslips 24h before analyzing with a confocal microscope (Andromeda-iMIC). Where indicated, cells were incubated with Picogreen (Life Technology; Cat. # P7589) (1:800) in complete DMEM for 40 min in 5% CO_2 at 37°C before visualization. For images acquisition DMEM was replaced with Hanks' Balanced Salt Solution (HBSS; Gibco, Cat. # 14025-050). For each cell, 40 Z-stacks (every 0.2 μm) were acquired and then analyzed with the ImageJ plugin MitoLoc,[48] to evaluate mitochondrial volume and fragmentation index. The fragmentation index was calculated as the percentage of the mitochondrial network smaller than 20% of the total mitochondrial volume. The nucleoid number was quantified from the 3D reconstruction using the ImageJ plugin Volume-J and analyzed with the ''Analyze Particle'' function. Data were normalized on mitochondrial volume.

Coimmunoprecipitation

For the Co-IP of the endogenous ATAD3A mitochondria isolated from mouse heart were lysed in RIPA buffer (50 mM Tris-HCl, 150 mM NaCl, 1% NP-40, 0.25% DOC, 1mM EDTA, pH 8.0) in the presence of protease inhibitor cocktail (PIC, Sigma, Cat.# PI8340). Then, 900 μg of lysate was incubated with 40 with μl of Protein-A magnetic beads (Invitrogen, Cat. # 10004D) coupled with the indicated antibodies overnight at 4°C. The beads were then collected and washed three times with TBS (20mM Tris, 150 mM NaCl, pH 7.4) to be then resuspended in LB 2X sample buffer and boiled before loading in NuPAGE Precast SDS-PAGE (Invitrogen). For the Co-IP of the HA tagged ATAD3A, protein lysates from MAFs ATAD3A-HA were obtained as indicated above. Lysate (final concentration 3mg/ml) was incubated (2h, RT) with 40 μl of beads conjugated or not with the HA antibody (Pierce; Cat. # 88836). Beads were washed and resuspended in LB2X as indicated for the endogenous protein.

Chemical crosslinking

Cells ($2x10^6$) or isolated mitochondria (200μg) were incubated with 10 mM 1-Ethyl-3-(3-dimethylaminopropyl) carbodiimide-HCl (EDC; Pierce; Cat. # 22980) in 200 μl PBS or mitochondrial EB, respectively, at R.T. Cells or mitochondria were then pelleted at 7500 x *g* or 1000 x *g*, respectively. Protein fraction from cells was extracted in RIPA buffer, quantified, and processed for SDS-PAGE, while mitochondria were directly resuspended in LB 2X sample buffer.

Immunofluorescence

Cells were seeded in a 12 well plate on a glass coverslip and transfected with the indicated plasmids and siRNA oligos as indicated. After 24-36h, cells were washed twice with PBS, fixed with 3,7% PFA, 20 min. After washing with PBS (3 x 5 min), cells were permeabilized with 0,1% Triton-X100 (Sigma; Cat. # T8787) for 20 min. After washing with PBS, cells were incubated with blocking buffer (10% goat serum, 2% BSA in PBS) for 30 min and incubated O/N with HA antibodies (1:2000) (Sigma; Cat. # H3663). After washing (4 x 5 min), cells were incubated with a goat anti-mouse IgG secondary antibody conjugated with Alexa Fluor 488 (1:10000) (Thermo Fisher Scientific; Cat. # A-11029) and a donkey anti-rabbit IgG secondary antibody conjugated with Alexa Fluor 647 (1:10,000) (Thermo Fisher Scientific; Cat. # A-31573), 1 h at dark, RT. After washing with PBS and an additional wash in water, the coverslips were mounted with ProLong Gold antifade (Invitrogen; Cat. # P36930).

Mitochondrial oxygen consumption

Mitochondria isolated (150μg) from MAFs silenced or not for ATAD3A and transduced with retroviruses expressing the ATAD3A or mutants as described above were added in 300 μl EB inside the Oxytherm electrode chamber (Oxytherm 1447 Hansatech Instruments Ltd), at 25°C. After 2 minutes, 200 μM ADP (Sigma, Cat. # A5285) was added to measure the State 3 respiration for 2 min. State 4 was reached after the addition of 1.3 μM oligomycin (Sigma, Cat.# O4876), and uncoupled respiration was studied by adding 25 μM 2,4-Dinitrophenol (DNP, Sigma, Cat #D198501). Respiratory Control Rate (RCR) was calculated as State 3 / State 4 respiration.

mtDNA quantification

Mouse mtDNA copy number was determined using the TaqMan probe system (Taq Man Universal PCR Master MIX, Applied Biosystems, 4304437) and Applied Biosystem 7500 real-time PCR as described in Frangini et al.[47] In detail, genomic DNA was extracted with the DNeasy Blood and Tissue Kit (QIAGEN; 69506) from MAFs silenced or not for ATAD3A and transduced with retroviruses expressing the ATAD3A or mutants. The mitochondrial cytochrome c oxidase subunit I TaqMan probe (6FAM-5 -TACTACTAACA GACC-3 -MGB; Applied Biosystems) and the primers (forward:5-TGCTAGCCGCAGGCATTACT-3; reverse:5 -CGGGATCAAA GAAAGTTGTGTTT-3) were used to quantify mtDNA. For the nuclear DNA, the actin (ACTB) primers and probe contained in TaqMan predeveloped assay (Applied Biosystems; 4352341E) were used. Nuclear DNA and mtDNA were determined using calibration curves generated by serial dilution of a mixture of plasmids carrying the two PCR amplicons. Each DNA sample has been analyzed in triplicate.

Sucrose gradient fractionation

Sucrose gradient was generated freezing four different layers (3 ml each) of 40%, 30%, 20% and 10% sucrose solution (10 mM Tris, 10 mM $MgCl_2$, 25 mM NaCl) in an ultracentrifuge tube. Then, the tubes with the frozen layers were left O/N at 4°C to allow the formation of a continuous gradient. Then, 400 μg (1 ml) of cell protein lysate were loaded on the top of the gradient and centrifuged at 33100 RPM in a SW40 rotor, 12 h at 4°C. After centrifugation, the five initial fractions of 1 ml each were collected, and 500 μl fractions were collected for the rest of the gradient (21 fractions in total). After TCA precipitation of 500 μl from each phase and two washes with acetone, the proteins were resuspended in LB buffer and the indicated fractions were loaded in a SDS-PAGE. For all the experimental conditions indicated, the gels were run, transferred, incubated, and immunodetected in parallel. To quantify the protein levels of MRPS22 and MRPL13, the O.D. of each fraction was normalized to the sum of the O.D. obtained in all the fractions from the same sample. ATAD3A levels for the scr+EV sample were normalized as for MRPS22 and MRPL13. For the rest of the experimental conditions, ATAD3A total levels were first normalized to the total ATAD3A of the scr+EV, and then protein levels in each fraction were again normalized to the percentage of the total ATAD3A of the same sample.

Bioinformatic model

The mouse Atad3a isoform 1 (UniProt: Q925I1) model was built using the homology modeling protocol implemented in the MOE suite (Molecular Operating environment; http://www.chemcomp.com). A multiple template strategy was achieved by selecting the most appropriate template for different protein regions using Hidden Markov Model profiles (HMMs) comparison from HHpred. The first 35 amino acids were excluded from the model generation since identified as mitochondrial targeting sequence according to MitoFates server. The following templates were retrieved from the Protein Bata Bank (www.pdb.it): 6B5C for the ATPase domain (region 306-560; Probability: 99.72%, E-value: 2.4e-15, Score: 153.25, Identities: 21%). While for the N-terminal region including the two coiled-coil regions and the trans membrane portion the structure 5ZUI (Probability: 99.33%, E-value: 2.1e-8, Score: 116.77, Aligned cols: 393, Identities: 20%) 59-540. Despite the structure 6B5C was the 3rd entry according HHprep score it was selected due to the highest resolution. The structure 5ZUI was the best scoring entry also covering the N-terminal region. The experimentally derived templates were prepared with the MOE structure preparation tool to add hydrogen atoms, fix missing atoms, and assign partial charges, and finally superposed. The homology model was obtained generating 10 different models using Amber12 Force Field and selecting the

best one according to the GB/VI score. The AlphaFold predicted structure AF-Q925I1-F1 was retrieved to assess the agreement between the two methodologies.

Blots quantification and statistical analysis

The O.D. intensities of western blot bands were quantified using ImageJ GelPro Analyzer. Statistical tests used in this study are specified in the figure captions and were calculated with OriginPro, Version 2022. OriginLab Corporation, Northampton, MA, USA.

ADDITIONAL RESOURCES

MARIGOLD and MitoCIAO webpage: https://mitociao.bio.unipd.it/